Journal of Optoelectronics and Advanced Materials Vol. 3, No. 4, December 2001, p. 779 – 816

REVIEW PAPER

THERMAL WAVES PHYSICS

R. Li Voti, G. L. Liakhou[a], S. Paoloni, C. Sibilia, M. Bertolotti

INFM and Dipartimento di Energetica, Università degli Studi di Roma "La Sapienza", Via Scarpa 16, 00161, Roma, Italy
[a]Technical University of Moldova, Stefan Cel Mare 168, 277012 Kishinau, Moldova

This article recalls the basic theory of thermal waves, analyses the main thermal waves phenomena, and discusses some clear applications to the nondestructive testing of materials by using photothermal techniques.

(Received April 5, 2001; accepted November 29, 2001)

Keywords: Thermal waves, Photothermal techniques, Thermal diffusivity, Thickness measurements, Hardness depth profiling

1. Thermal waves

The word "*thermal wave"* commonly refers to the typical wave-like temperature field that is induced by a harmonic heating process. These waves were already used by Lord Kelvin and A.J. Ångström to investigate the thermal diffusivity of bodies, but only recently, in the early 80's, have been called "*thermal waves*", arousing a remarkable clamour [1-4]. Presently the scientific community still debates on the real nature of thermal waves, even if their formalism is widely accepted and used to describe the temperature field in periodical regime. In the following we want to recall the basic theory and discuss some fundamental phenomena as the *thermal wave reflection and refraction*, the *thermal wave interferometry*, the *thermal wave resonance*, and the *thermal wave scattering,* together with the main relative applications.

The fundamental point to be understood is how the heat conduction could show a wave-like behaviour. Heat conduction, as it is well known is the classical case of a diffusive process, as shown by the Fourier equation

$$\nabla^2 T - \frac{1}{D}\frac{\partial T}{\partial t} = -\frac{w}{k} \tag{1}$$

where *k* and *D* are respectively the thermal conductivity and diffusivity of the medium, and *w* is the heat supplied per unit time per unit volume. The Green function solution of Eq.(1) for a unitary heating pulse placed in the origin *O* at time *t=0,* that is [5,6]

$$G_1(x,y,z,t) = \frac{1}{8\rho c[\pi D t]^{3/2}} e^{-\left(x^2+y^2+z^2\right)/\,4Dt} \qquad t>0 \tag{2}$$

where ρc is the heat capacity per unit volume, shows clearly the diffusive behavior.

A different situation is found in the case of harmonic heating. If the quantity *w* is harmonic in time, with the period $2\pi/\omega$, the temperature field *T* is forced to be harmonic with the same periodicity. By introducing in Eq.(1) the complex quantities $\tilde{w}$ and $\tilde{T}$, so that $w = \mathrm{Re}\left[\tilde{w}e^{j\omega t}\right]$ and $T = \mathrm{Re}\left[\tilde{T}e^{j\omega t}\right]$, one obtains the Fourier equation in harmonic regime [5-7]

$$\nabla^2 \tilde{T} - \beta^2 \tilde{T} = -\frac{\tilde{w}}{k}, \tag{3}$$

where the analogy between Eq.(3) and the Helmoltz wave equation has been put into evidence by introducing the wave number $\beta = \sqrt{j\omega/D}$. As a consequence one may apply the well-known theory of the wave physics even to the harmonic thermal field.

As an example we want to study the Green function solution of Eq. (3) for the unitary harmonic point source in the origin *O*, that is [5-7]

$$\begin{aligned} \widetilde{G}_2(r,\omega) &= \frac{e^{-\beta r}}{4\pi k r} = \frac{e^{-(1+j)r/\ell}}{4\pi k r} \\ G_2(r,t) &= \mathrm{Re}\left[\widetilde{G}_2(r,\omega)e^{j\omega t}\right] = \frac{e^{-r/\ell}}{4\pi k r}\cos(\omega t - r/\ell) \end{aligned} \quad , \tag{4}$$

where *r* is the distance from the origin, and ℓ is the thermal diffusion length defined as $\ell = \sqrt{2D/\omega}$. By a first inspection of Eq.(4) one may notice that the temperature field G_2 behaves as a spherical wave of wavelength $2\pi\ell$, and, for this reason, has been called "*thermal wave*". The main characteristic of such a wave is that it decays strongly, moving away from the heating source (see the exponential term in Eq.4). In practice the *thermal wave* vanishes within some wavelengths so that many authors still debate on the use of the term "*wave*". The damping is driven by the wavenumber $\beta=(1+j)/\ell$. It is a complex quantity with the same real and imaginary part. As a consequence the thermal diffusion length ℓ plays a double role: from one side it is proportional to the thermal wavelength $2\pi\ell$, and from the other side it represents the extinction length at which the exponential term in Eq.(4) is reduced to *1/e* of its initial value.

Once we have introduced the *spherical thermal wave* G_2, it can be used to describe any harmonic field *T* which may always result from an appropriate superposition of *spherical thermal waves* sprung from the heating sources. Analogously we could introduce the *plane thermal wave* when the heating sources are arranged along a plane. By heating harmonically and homogeneously the medium along the plane *xy*, *T* assumes the shape of a *plane thermal wave* propagating in the *z* direction, as follows [5-7]

$$\begin{aligned} \widetilde{T}(z,\omega) &= Ae^{-\vec{\beta}\cdot\vec{r}} = Ae^{-\beta z} = Ae^{-(1+j)z/\ell} \\ T(z,t) &= \mathrm{Re}\left[\widetilde{T}(z,\omega)e^{j\omega t}\right] = Ae^{-z/\ell}\cos(\omega t - z/\ell) \end{aligned} \quad , \tag{5}$$

A being the amplitude at *z=0,* and $\vec{\beta}$ the wavevector which points the direction of propagation. The plane thermal wave in Eq. (5) is plotted in Fig. 1 as a function of the distance *z*, for different values of the time: in particular the curves *a,b,c,d* correspond to $\omega t = 0, \pi/3, \pi/2, \pi$. As the time goes on, the maximum temperature rise is reduced but moves in the *z* direction, like a forward damped wave. Note that, at any time, the temperature oscillates within the two exponential envelopes $\pm\exp[-z/\ell]$, that limit the thermal wave range. The difference between spherical and plane thermal waves is merely geometrical and does not affect the general properties just shown; in particular any field *T* may always be also decomposed in terms of *plane thermal waves* propagating in various directions.

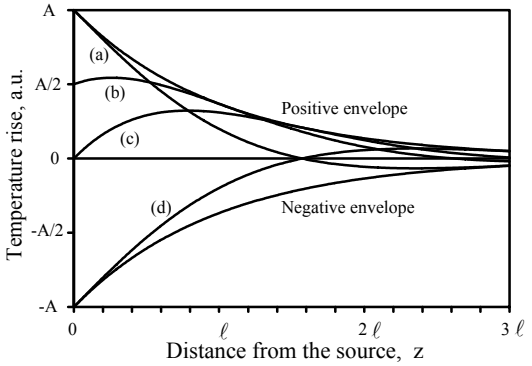

Fig. 1. Example of plane thermal wave. The temperature rise is plotted vs the distance *z* (in ℓ unit), for different value of the time: curves *a,b,c,d* respectively correspond to $\omega t = 0, \pi/3, \pi/2, \pi$. The two envelopes represents the maximum and the minimum values of

the temperature rise.

2. Thermal wave reflectin and refraction

Besides the thermal wave generation and propagation in a homogeneous medium, other basic phenomena should be observed when at least two media are involved: the *reflection* and the *refraction* [7-9]. In the following we will discuss these phenomena, without lack of generality, for plane thermal waves.

When a plane thermal wave approaches the interface between two media (i.e the plane $z=0$), it is partially reflected back and refracted beyond. By imposing the continuity at the interface of both the field $\widetilde{T}$, and the vertical heat flux ($-k\,\partial\widetilde{T}/\partial z$) one obtains

$$\begin{cases} \widetilde{T}_1 = \widetilde{T}_2 \\ k_1 \dfrac{\partial \widetilde{T}_1}{\partial z} = k_2 \dfrac{\partial \widetilde{T}_2}{\partial z} \end{cases} \qquad (z=0), \tag{6}$$

where the fields in the first ($\widetilde{T}_1$) and in the second medium ($\widetilde{T}_2$) have been decomposed in terms of plane thermal waves as follows

$$\begin{cases} \widetilde{T}_1(x,z) = Ae^{-\beta_1[sin(\theta_1)x+\cos(\theta_1)z]} + rAe^{-\beta_1[sin(\theta_1')x-\cos(\theta_1')z]} \\ \widetilde{T}_2(x,z) = tAe^{-\beta_2[sin(\theta_2)x+\cos(\theta_2)z]} \end{cases}, \tag{7}$$

where A, rA and tA respectively are the amplitudes of the incident, reflected and refracted waves, while θ_1 , θ_1' and θ_2 are the angles between the directions of the waves and the normal to the interface. By combining Eqs.(6) with Eqs. (7) one obtains the Snell relationships for the angles

$$\begin{cases} \theta_1' = \theta_1 \\ \dfrac{1}{\sqrt{D_1}} sin(\theta_1) = \dfrac{1}{\sqrt{D_2}} sin(\theta_2) \end{cases}, \tag{8}$$

and the relationships for the reflection (r) and the transmission (t) coefficients

$$r = \frac{e_1 \cos(\theta_1) - e_2 \cos(\theta_2)}{e_1 \cos(\theta_1) + e_2 \cos(\theta_2)}$$

$$t = r + 1 = \frac{2e_1 \cos(\theta_1)}{e_1 \cos(\theta_1) + e_2 \cos(\theta_2)} \tag{9}$$

$e = k/\sqrt{D}$ being the thermal effusivity. Note that in the case of $D_2>D_1$ the Snell law is valid only until $\theta_1 \le arcsin\left(\sqrt{D_1/D_2}\right)$ (see Eq. 8). For larger values of θ_1 the thermal waves in the second medium become inhomogeneous (the planes at constant phase differ by the planes at constant amplitude) [9]. Although such waves have been not yet observed, the theory predicts for them an anomalous attenuation larger than the one described in Eq. (5), as will be discussed later. Eq. (9) gives the coefficients r and t, and consequently, the efficiency of the heat transfer through the two media. Generally the reflection (r) and transmission (t) depend mainly on the effusivity mismatch, but also on the diffusivity mismatch (in fact the term $\cos(\theta_2)$ in Eq. (9) is linked to diffusivity by Eq. (8)); one

exception is for normal incidence ($\theta_1 = \theta_2 = 0$) where *r* and *t* depend on effusivity only. In Fig. 2 both coefficients are plotted vs the effusivity ratio e_2/e_1, just for normal incidence.

2.1 Thermal wave mirror

If the effusivity mismatch between the media is very high, a relevant reflection phenomenon takes place (see Fig. 2) whether in phase, for very small e_2/e_1, or in opposition of phase, for very large e_2/e_1 [10]. In both cases the second medium behaves as a "*thermal wave mirror*" ($r \to \pm 1$); but the transmission, that is always *t=r+1*, in one case tends to 2, in the other tends to 0. As an example we consider the interface between a generic gas and a generic solid. Since any solid is always at least 100 times more effusive than any gas, the effusivity mismatch is extremely high, and consequently, the solid behaves as a *thermal wave mirror* for the gas and vice versa for reciprocity, but with the following differences:

(a) if the incident wave is coming from the gas, the effusivity ratio is $e_2/e_1>100$, the reflection $r \to -1$, and the transmission $t \to 0$; in synthesis in the gas takes place a destructive interference between incident and reflected waves, at the interface the temperature rise is kept to zero, and in the solid there is no relevant energy transfer.

(b) if the incident wave is coming from the solid, the effusivity ratio is $e_2/e_1<0.01$, the reflection $r \to 1$, and the transmission $t \to 2$; in synthesis in the solid takes place a constructive interference between incident and reflected waves, at the interface there is the maximum temperature rise, and in the gas there is the maximum energy transfer.

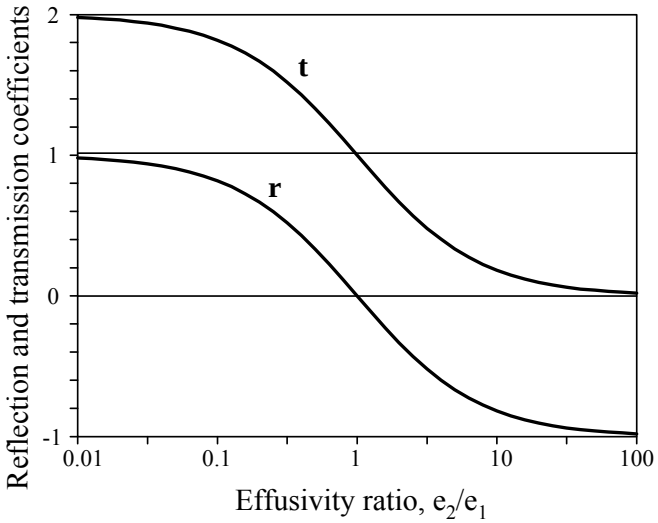

Fig. 2. The thermal reflection and transmission coefficients between the media No.1 and No.2 are plotted vs the thermal effusivity ratio e_2/e_1.

Just to conclude this theoretical discussion, it is of practical interest to understand which is the appropriate depth for a *thermal wave mirror*, or, in other words, which is the lower limit for the thickness of a material, beyond which the reflection properties are lost. An advanced study on the layered structures has recently put into evidence how the reflection properties of a slab change with its thickness. If R_∞ is the reflection for an infinite thick slab, the effective reflection *R* for a finite slab differs by R_∞ as follows [7,10].

$$R = R_\infty \cdot \frac{1 - \exp\left[-2(1+j)d/\ell\right]}{1 - R_\infty^2 \cdot \exp\left[-2(1+j)d/\ell\right]} \tag{10}$$

where d is the thickness of the slab. Note once again the perfect analogy between Eq. (10) and the equations for the Fabry-Perot interferometer in the wave physics; in our case, a thermal wave interference occurs in the slab, which may whether enhance (constructive interference) or inhibit (destructive interference) the effective reflection R with respect to R_∞. In order to study the efficiency of such *thermal wave mirror*, in Fig. 3 we plot $|R/R_\infty|$ as a function of the normalized thickness defined as $\left(\frac{d}{\ell}\cdot\frac{|R_\infty|}{1-R_\infty^2}\right)$, for different values of $|R_\infty|$ (*0.2, 0.5, 0.9, 0.99, 0.999*). Note that all curves merge together in the two following opposite limits:

(a) for a high normalized thickness the slab is thermally thick, behaves as an infinite medium, and consequently $R \to R_\infty$ (mirror regime);

(b) for a low normalized thickness the slab is thermally too thin, the incident thermal wave is transmitted beyond the slab, without a relevant reflection $R \to 0$ (transparent window).

Note also that the transition from transparent to mirror regime occurs when the normalized thickness is practically unitary, which, for a high effusivity mismatch $(|R_\infty| \approx 1)$, corresponds even to an extremely small thickness $d \approx \ell \cdot \left(1 - R_\infty^2\right)$. This is the reason why even extremely small defects, cracks, and delaminations, behave as thermal wave mirrors, and may be easily detected by the thermal wave interfererometry [11,12].

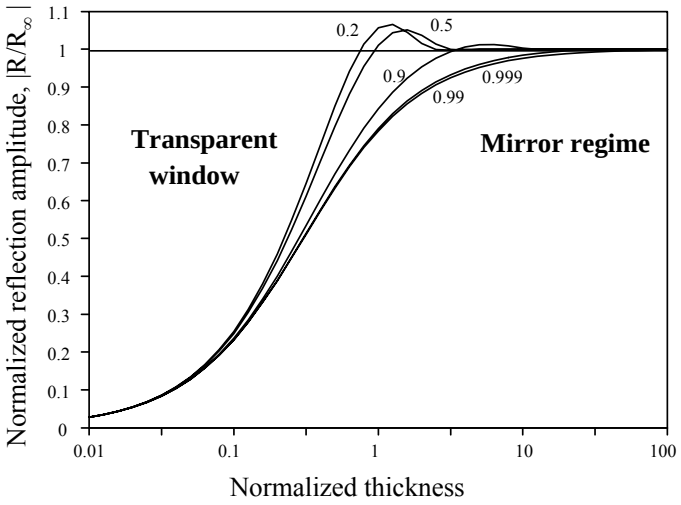

Fig. 3. The normalized thermal reflection $|R/R_\infty|$ of a slab is plotted vs the normalized thickness for different values of the interface reflection coefficient R_∞ (0.2, 0.5, 0.9, 0.99, 0.999). The normalized thickness is defined as $\left(\frac{|R_\infty|}{1-R_\infty^2}\right)\frac{d}{\ell}$ where ℓ is the slab thermal diffusion length.

2.2 Evidence of the thermal wave reflection

A simple experiment to prove the reflection of thermal waves is shown in Fig. 4. A plane thermal wave is generated in air by heating periodically a thin absorbing layer with a wide pump laser beam (s = 4mm). The plane wave propagates in air along z for a short distance (L = 1mm) till approaches the aluminium foil which acts as a thermal wave mirror. The foil lies obliquely so to form the angle θ with the x axes. As a consequence the reflected wave forms an angle 2θ with the incident one, and the temperature rise in air calculated where the waves are superimposed is [9]

$$\widetilde{T}_{air}(x,z) = Ae^{-\beta_{air} z} + R \cdot Ae^{\beta_{air}[\cos(2\theta)z - \sin(2\theta)x]} \tag{11}$$

where A is the amplitude of the incident wave in the origin O, and R is given by Eqs. (9) and (10). The detection of the thermal field in Eq. (11) may be obtained for example by using the *mirage technique* [13-17]. A probe beam is sent along the y axis, in air, close to the origin O. The thermal gradients met along the path produce the beam deflection which is measured by a remote position sensor. In particular its orientation is chosen so to detect the components of the deflection angle along the x and z directions which are given by [9,10]

$$\begin{aligned} \Phi_x &= \frac{1}{n}\left(\frac{dn}{dT}\right)\int_y \frac{\partial T_{air}}{\partial x}\,dy = \frac{1}{n}\left(\frac{dn}{dT}\right)L_{eff}\,\frac{\partial T_{air}}{\partial x} \\ \Phi_z &= \frac{1}{n}\left(\frac{dn}{dT}\right)\int_y \frac{\partial T_{air}}{\partial z}\,dy = \frac{1}{n}\left(\frac{dn}{dT}\right)L_{eff}\,\frac{\partial T_{air}}{\partial z} \end{aligned}, \tag{12}$$

where n, dn/dT respectively are the air refractive index and the air optothermal coefficient, and L_{eff} is the effective length useful for the beam deflection, which depends on the lateral dimensions s of the incident thermal wave. By combining Eqs. (11) and (12) one obtains

$$\begin{aligned} \widetilde{\Phi}_x &= C\ \left[R\sin(2\theta)e^{\beta_{air}[\cos(2\theta)z - \sin(2\theta)x]}\right] \cong C\ \left[R\sin(2\theta)\right] \\ \widetilde{\Phi}_z &= C\ \left[e^{-\beta_{air} z} - R\cos(2\theta)e^{\beta_{air}[\cos(2\theta)z - \sin(2\theta)x]}\right] \cong C\ \left[1 - R\cos(2\theta)\right] \end{aligned} \tag{13}$$

where C is a constant defined as $C = -\frac{1}{n}\left(\frac{dn}{dT}\right)L_{eff}\beta_{air}A$. Note that the simplifications in the exponential terms in Eq. (13) are allowed if the probe beam travels close to the origin O, at a shorter distance than ℓ_{air}. In such a case the two components are proportional to each other, and their ratio Ω depends only on the angle θ and on the reflection coefficient of the mirror R as follows

$$\Omega = \frac{\widetilde{\Phi}_x}{\widetilde{\Phi}_z} = \frac{R\sin(2\theta)}{1 - R\cos(2\theta)} \cong \frac{-\sin(2\theta)}{1 + \cos(2\theta)} = -tg(\theta). \tag{14}$$

In Eq.(14) we have assumed $R \approx -1$ because the aluminium foil, for any θ, acts as a thermal wave mirror (see Eqs. 9, 10). The experiment has been performed in the *thermal wave cavity* described in Fig. 4, where the tilt angle θ between the mirror and the absorbing layer has been set at θ=*11*°. Both components $\widetilde{\Phi}_x$ and $\widetilde{\Phi}_z$ have been measured and their ratio Ω has been compared with Eq.(14). The results have been repeated by changing the modulation frequency f (i.e. ℓ_{air}). In Fig. 5 the amplitude ratio |Ω| is plotted as a function of $\sqrt{f}$; the symbols represent the experimental data, the full lines are the theoretical values by Eq. (14) for the tilt angles θ reported on the right scale (0°-5°-10°-11°-15°). Note that the experimental points lie, with some noise, on the line at θ=11°, at any frequency. This agreement proves the following points:

(a) The reflection phenomenon takes place as described by Eq. (11)
(b) The aluminium foil acts as a thermal wave mirror for a wide spectrum of the thermal wavelength (i.e. ℓ_{air}).

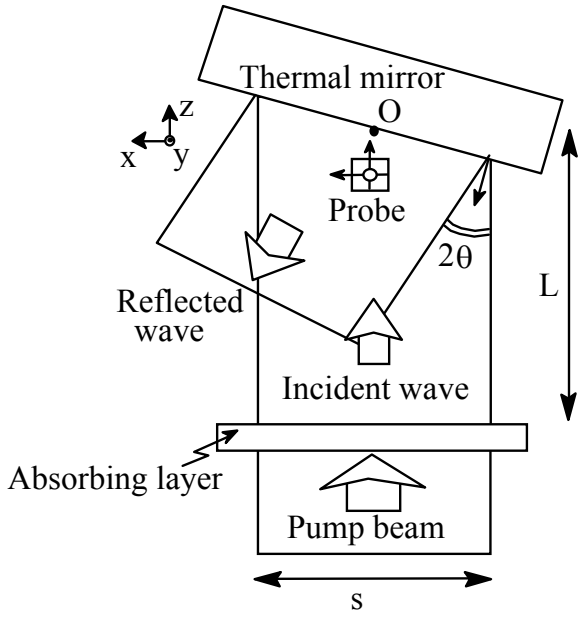

Fig. 4. Scheme of the thermal wave cavity for the detection of the reflected thermal wave.

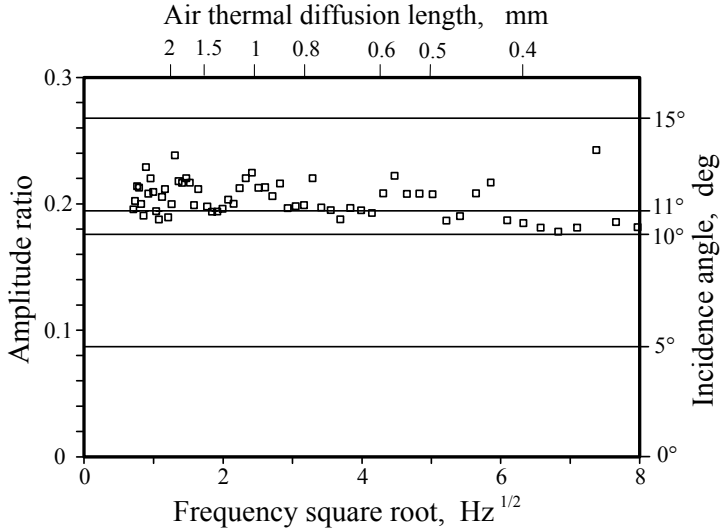

Fig. 5. The amplitude ratio Ω between the deflection components along *x* and *z* is plotted vs the modulation frequency square root: the open square symbols (□) represent the experimental points, while full lines are calculated by Eq. (14) for different values of the tilt angles θ as

shown in the right scale.

2.3 Evidence of the thermal wave refraction

Besides the proof of the thermal wave reflection, an experiment may be set up to prove the refraction of the thermal waves as shown in Fig. 6. The pump laser beam propagates along *y*, is modulated in time and focused onto a solid sample (medium 1) by means of a cylindrical lens. The dimensions of the ellipsoidal pump beam spot in the plane *xz* (see Fig. 4) are adjusted so to realise, at the best one can, a line heating source along *x*. The generated thermal wave propagates along *z* inside the solid until it reaches the interface with the second medium (air) which is placed obliquely with respect to the line source (the normal to the interface *n* forms the angle θ_1 with the *z* axis). Therefore

the theory predicts that the incident wave is reflected back and refracted in the second medium according to Eqs. (7) and (8). For the thermal field refracted in the second medium one may write [9]

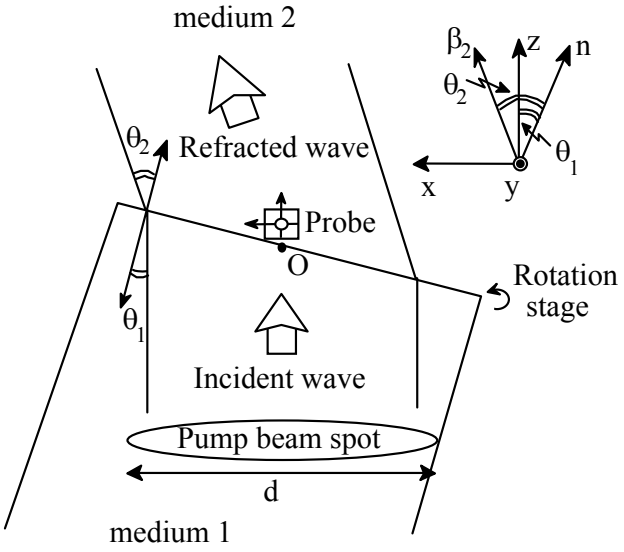

Fig. 6. Schematic set-up for the detection of the refracted thermal wave.

$$\widetilde{T}_2(x,z) = tAe^{-\vec{\beta}_2\vec{r}} = tAe^{-\beta_2[sin(\theta_2-\theta_1)x+\cos(\theta_2-\theta_1)z]} \tag{15}$$

where A is again the amplitude of the incident wave in the origin O, t is the transmission coefficient given in Eq. (9), $\vec{r}$ is the position with respect to O, $\vec{\beta}_2$ is the wavevector which points the direction of the refracted thermal wave, θ_2 is the refraction angle between $\vec{\beta}_2$ and the normal to the interface n. In Eq. (15) the quantity $\widetilde{T}_2$ is expressed as a function of x and z which are the reference axes. Note that in such reference system the direction of the refracted wave $\vec{\beta}_2$ forms the angle θ_2-θ_1 with the z axis (see Fig. 6 and Eq. 15). The detection of the thermal field in Eq. (15) is given by the *mirage technique* , as in the previous experiment. The probe beam is placed in the second medium near the interface, where the heat flux is larger. The two components of the deflection angle along x and z are given by combining Eqs. (12) and (15) as follows [9]

$$\begin{aligned}\widetilde{\Phi}_x &= C\left[t\ \ \sin(\theta_2-\theta_1)\ \ e^{-\beta_2[\sin(\theta_2-\theta_1)x+\cos(\theta_2-\theta_1)z]}\right]\\ \widetilde{\Phi}_z &= C\left[t\ \ \cos(\theta_2-\theta_1)\ \ e^{-\beta_2[\sin(\theta_2-\theta_1)x+\cos(\theta_2-\theta_1)z]}\right]\end{aligned} \tag{16}$$

Note that in this case the two components are proportional to each other everywhere, whatever x and z, and their ratio depends only on the incidence and refracted angles

$$\Omega = \frac{\widetilde{\Phi}_x}{\widetilde{\Phi}_z} = tg(\theta_2-\theta_1) \tag{17}$$

By looking at the analogy between Eqs. (14) and (17), one concludes that the amplitude ratio Ω is useful not only to detect simply the thermal wave, but also to reveal exactly its direction. The physical reason is in the basic principle of the *mirage technique*: the deflection angle is related not directly to the temperature field $\widetilde{T}$, but rather to its gradient $\nabla\widetilde{T}$ which points the direction of the heat flux. Therefore if one is interested in the direction of a thermal wave, the knowledge of the scalar

function $\widetilde{T}$, even if at any plane, could be helpless, while the vectorial field $\nabla\widetilde{T}$ gives immediately such information, point by point. Therefore the *mirage* represents the most appropriate technique for this purpose. In particular the ratio between the components $\widetilde{\Phi}_x$ and $\widetilde{\Phi}_z$ gives, as previously shown, the local information on the angle between $\vec{\beta}_2$ and the *z* axis. Coming back to the differences between Eq. (14) and Eq. (17), an important point is the sign of Ω. In the reflection experiment it is always negative, while in the refraction experiment it depends on the sign of θ_2-θ_1 , which is fixed by the Snell law (see Eq. 8). As a result if $D_2>D_1$, then $\theta_2>\theta_1$ and consequently $\Omega>0$, while if $D_2<D_1$ then $\Omega<0$. The sign of Ω helps to discriminate one case from the other. The knowledge of Ω allows to calculate the refraction angle θ_2 by solving Eq.(17) as follows

$$\theta_2 = \theta_1 + \text{arctg}[\Omega(\theta_1)] \tag{18}$$

As an example we report the results obtained with the setup shown in Fig. 6. An Ar laser illuminates a flat solid sample (medium 1) not far from one edge. The pump beam modulated in time, is focused by a cylindrical lens only in the *z* direction so to have a line source 6mm wide along *x* and a few microns wide along *z*. A probe He-Ne laser collinear with the pump Ar laser is placed in air (medium 2) close to the sample edge. A rotation stage allows the movement of the sample in the *xz* plane, so to change the orientation of the edge. The pump and the probe are fixed. As a consequence the incidence angle θ_1 is changed by the rotation stage. In Fig. 7 the amplitudes of both $\widetilde{\Phi}_x, \widetilde{\Phi}_z$ are shown vs θ_1 for a semiconductor wafer of InP. From these experimental data one calculates the ratio Ω, and eventually, by using Eq. (18), the refraction angle θ_2. Finally by plotting the quantity $sin(\theta_2)$ vs $sin(\theta_1)$, one has the most appealing proof of the Snell law; in fact a straight line is expected, with the slope equal to $\sqrt{D_2/D_1}$ (see Eq. 8).

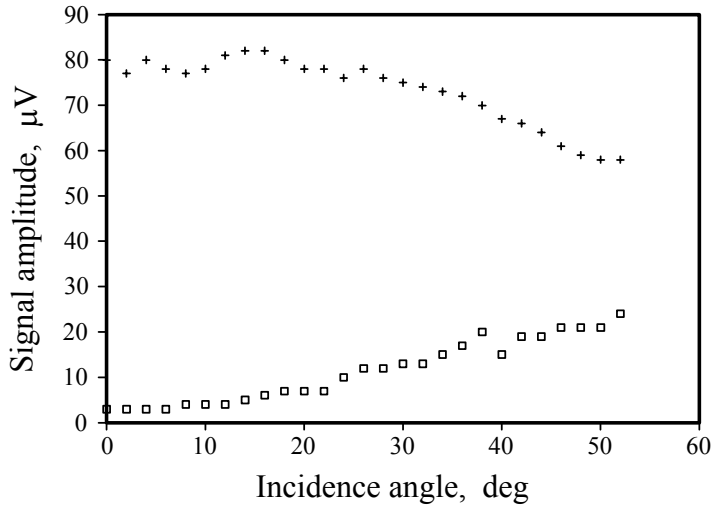

Fig. 7. The amplitude of the deflection signal (μV) is plotted versus the incidence angle (degree). The sample is a InP wafer. The pump power is 800mW, while the modulation frequency is f = 16Hz. In the plot (□) is for the component along *x*, while (+) is for the component along *z*.

In Fig. 8 this procedure is reported for two materials: one less diffusive than the air (Invar □) and the other more diffusive (InP +). Note that in the first case the linear behaviour is broken around $\theta_1 \approx 30°$, which corresponds to the limit angle $\theta_{\text{lim}} = arcsin\left(\sqrt{D_1/D_2}\right)$. Beyond the limit angle Eqs. (8) and (18) become useless and, as a consequence, the experimental points measured for $\theta_1 > 30°$, for the invar sample only, are meaningless. By using the least square method to calculate the slopes (see

full lines in Fig. 8) one obtains the diffusivity ratios D_{InP}/D_{air} =2.2 ± 0.1 and D_{invar}/D_{air} =0.25 ± 0.02 which

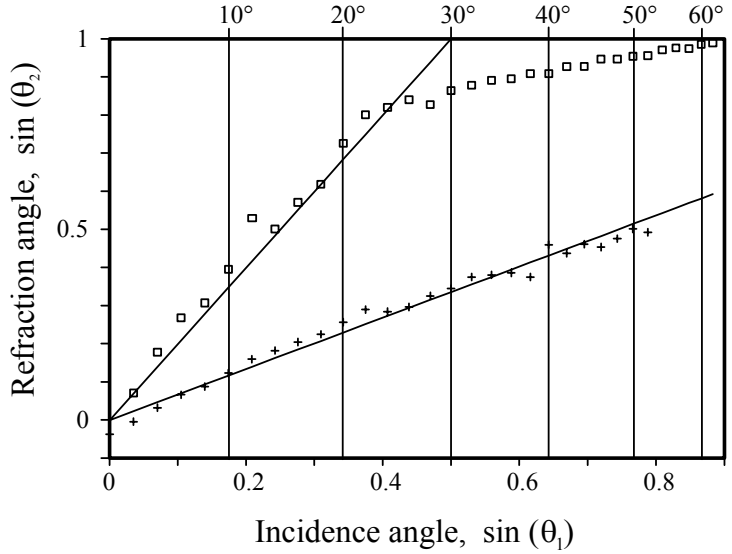

Fig. 8. The quantity $\sin(\theta_2)$ is plotted vs $\sin(\theta_1)$ for two different materials. The symbols are for the experimental results on a invar sample (□), and on a InP semiconductor wafer (+). The full lines are given by the least square method.

lead to the values D_{InP}=0.44 cm^2/s, and D_{invar}=0.05 cm^2/s , when one assumes D_{air}=0.2 cm^2/s, in perfect agreement with the values given in the literature [18]. Has been here introduced a new methodology to determine the thermal diffusivity of materials? Reasonable question, but difficult to answer! We limit to underline three points:

(a) This method based on the Snell law allows to determine the thermal diffusivity of one medium if the other's one is well known.
(b) This method works wherever is the heating source, whether in the first or in the second medium: therefore it is suitable even for measuring the diffusivity of non absorbing materials.
(c) Preliminary results indicate that this method guarantees the same accuracy than the other well-known methods [19-22].

2.4 Inhomogeneous thermal wave

The Snell law for thermal waves establishes that $1/\sqrt{D}$ plays the same role of the refractive index for electromagnetic waves. Due to this analogy, a simple question may be asked: is it also analogous of the total reflection also for thermal waves? The answer is in the refracted thermal field when the incidence angle is $\theta_1 > \theta_{lim}$. One may expect that the refracted thermal wave is still plane, but no more homogeneous, as one can see from the expression [8,9]

$$\widetilde{T}_{2\pm}(\rho,\zeta) = B \cdot \exp\left[-\frac{(1+j)}{\ell_1} sin(\theta_1)\rho \quad \pm \quad \frac{(1-j)}{\ell_2}\zeta\sqrt{\frac{D_2}{D_1} sin^2(\theta_1) - 1} \right], \tag{19}$$

where B is a constant, and ρ, ζ are respectively the variables parallel and vertical to the interface. In Eq. (19) two different solutions are included depending on the sign ± in the exponential term. Both of them satisfy the wave equation Eq. (6), but the solution $\widetilde{T}_{2+}$ may seem to be physically meaningless in the space $\zeta > 0$, because it is amplified in the direction ζ. To clarify this point it is helpful to study the amplitude of the field $\widetilde{T}$ for a simple system made of air and a low diffusivity material (invar).

The air is in the half space $\zeta > 0$, while the invar is for $\zeta < 0$. The heating source is an oblique line inside the material; the line begins from the origin O , and forms the angle θ_1 with $\zeta = 0$. The amplitude of the field $\tilde{T}(\rho,\zeta)$, calculated by a numerical simulation, is reported in the contour plots of Figs. 9 for two different values of the angle θ_1 chosen to induce homogeneous (see Fig. 9a) or inhomogeneous (see Figs. 9b,c) refracted thermal waves. In particular in Fig.9a the incidence angle is $\theta_1=20°<\theta_{lim}=30°$. Note that plane thermal waves depart from the heating line inside the material, as it is pointed out by the arrows. The wave propagating towards the air-invar interface is partially reflected back and refracted in air. As a consequence a thermal interference occurs just below the surface, where the incident and reflected wave are superimposed, as it is revealed by the strong distortion of the wave front. In air the refracted plane thermal wave changes direction according to the Snell law ($\theta_2=43°$), as pointed out by the arrows in Fig. 9a. Of course the refracted field is far to be a plane wave close to the origin O, due to the finite dimensions of the heating source, but these boundary effects vanish within a thermal diffusion length ℓ_2 [23]: in other words the refracted wave becomes plane at a suitable distance $\rho > \ell_2$.

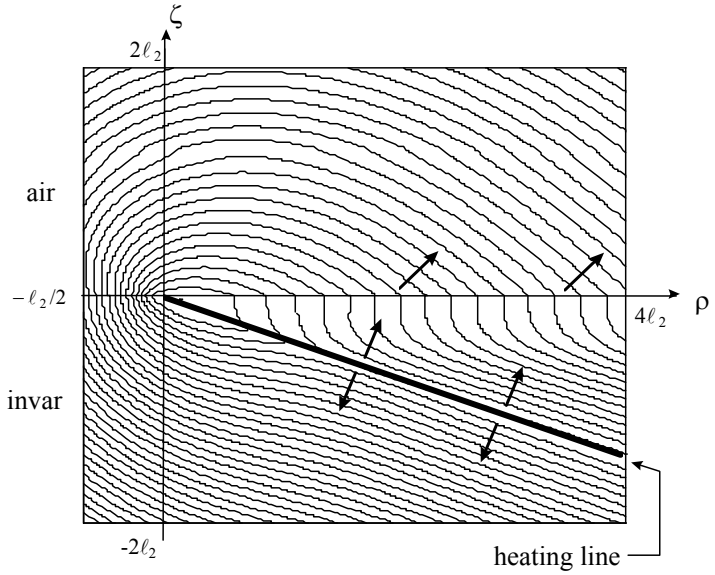

Fig. 9a. Numerical simulations for the amplitude of the thermal field. The countour plots of the amplitude of $\tilde{T}$ are calculated as a function of the coordinates ρ, ξ when an invar sample with

$D_1=0.05\ cm^2/s$ is heated by an oblique line source: $\theta_1=20°$

A different case is reported in Figs. 9b,c where $\theta_1=70°>\theta_{lim}=30°$. As the incident wave approaches the air-invar interface it is reflected back giving rise to the usual interference phenomenon. In air the thermal field is now far to be a plane wave (see Fig. 9b). However it is still possible to recognise a restricted region, close to the interface, where the amplitude tend to maintain a plane wavefront (see the arrows in Fig. 9c). In such a region the unstable solution $\tilde{T}_{2+}$ takes place instead of $\tilde{T}_{2-}$ and, as a consequence, the amplitude locally really increases with the height ζ. The physical reason is that in this zone the main heat flux comes from the higher air layers rather than from the inside material (see the arrows in Fig. 9c). Unfortunately one could observe this inhomogeneus wave far from the origin ($\rho > 6\ell_2$) where the wave is too weak to be detected.

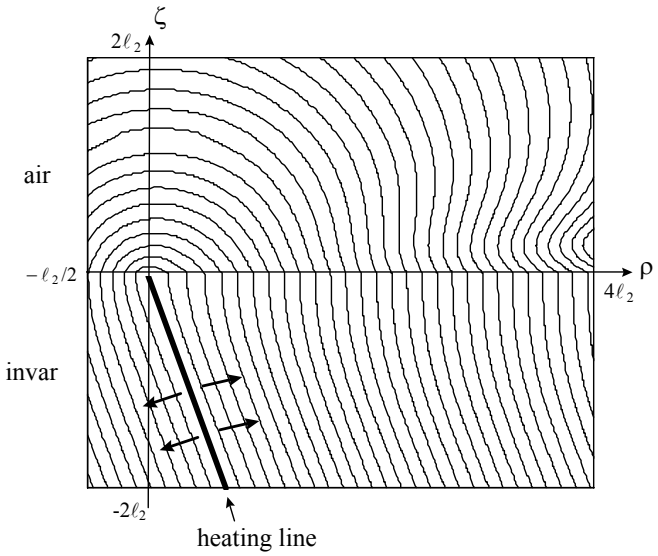

Fig. 9b. Same numerical simulation of Fig. 9a. The sample is now heated by an oblique line source at θ_1=70°.

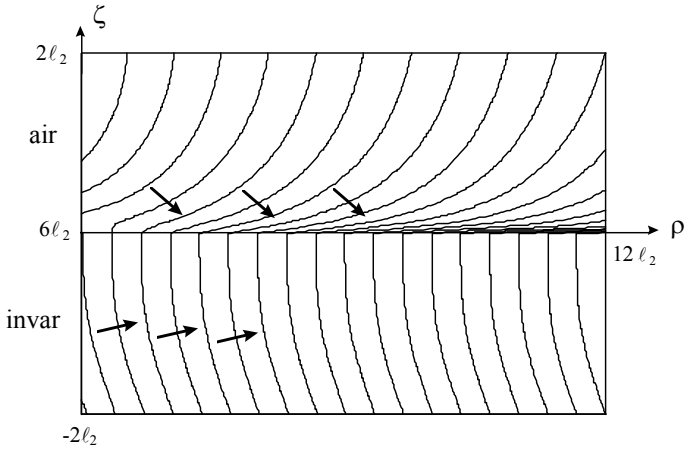

Fig. 9c. Extension of the contour plots of Fig. 9b for $6\ell_2 < \rho < 12\ell_2$.

3. Thermal wave interferometry

Thermal wave interferometry is commonly used for the nondestructive evaluation of the thickness in layered materials [3,7,24]. The basic principle is to illuminate an opaque specimen with a wide laser beam, periodically chopped at the frequency *f*, so to generate a plane thermal wave at the surface. This wave, travelling in the layered structure, is subjected to a multiple reflection phenomenon. As a conclusion, in the generic i[th] layer the following thermal wave interference takes place

$$\hat{T}_i(z) = A_i \cdot \exp[-z/\ell_i] + B_i \cdot \exp[z/\ell_i], \tag{20}$$

where $\ell_i = \sqrt{D_i/\pi f}$ is the thermal diffusion length of the i[th] layer, and the coefficients A_i and B_i should be determined by the boundary conditions at each interface (see *Thermal wave in layered materials*). To simplify the discussion, we consider now a two-layers system: an opaque thin coating over a substrate (see Fig. 10).

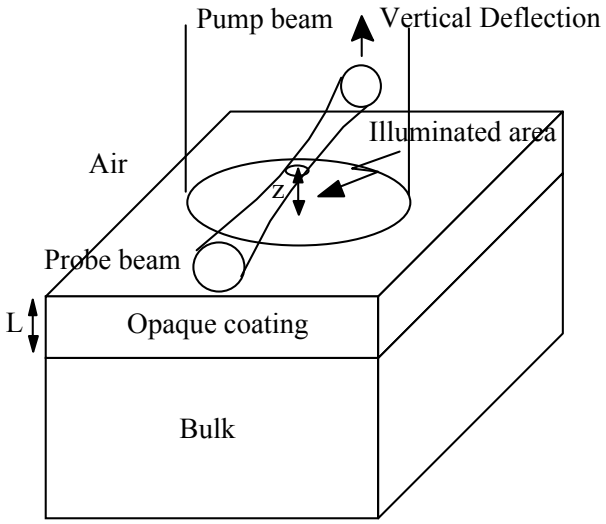

Fig. 10. Schematic set-up for the detection of the thermal wave interference in a two-layer system.

The plane wave is generated at the surface, propagates in the coating, approaches the rear interface (bulk) and is partially reflected back, then reaches the front surface (air) and is again partially reflected back, and so on, giving rise to a thermal wave interference. The surface temperature is (see *Thermal wave in layered materials*) [7,25]

$$\hat{T}_{surf} = \frac{I}{(e_c + e_{air})\sqrt{j\omega}} \cdot \left[\frac{1 + R_2 \exp[-2(1+j)L/\ell_c]}{1 - R_1 R_2 \exp[-2(1+j)L/\ell_c]} \right] \tag{21}$$

where $R_1 = \frac{e_c - e_{air}}{e_c + e_{air}} \approx 1$, and $R_2 = \frac{e_c - e_b}{e_c + e_b}$ respectively are the reflection coefficients at the front surface and at the rear interface, $e_{c/b/air}$ is the coating/bulk/air thermal effusivity, L is the coating thickness, ℓ_c is the coating thermal diffusion length, I is the thermal power deposited per unit area. The expression of the surface temperature in Eq. (21) may be seen as the product of two factors: the first represents the surface temperature of a "*thick coating*", without any interference effect; the second, in the square brackets, is the correction due to the thermal wave interference in the coating, which may enhance (constructive interference) or reduce (destructive interference) the surface temperature. This phenomenon is clearly seen in the damped oscillations of $\hat{T}_{surf}$, for both amplitude and phase, by simply changing the modulation frequency f that drives the normalized thickness $L/\ell_c = L\sqrt{\pi f / D_c}$ and consequently the interference pattern. One fundamental quantity, in thermal wave interferometry, is the *phase contrast* $\Delta\phi$ that compares the phase of Eq.(21) with the reference phase without interference (i.e. for infinite normalized thickness), as follows

$$\Delta\varphi = \varphi - \varphi_{ref} = -arc\tan\left(\frac{2R_2 \cdot sin(2L/\ell_c) \cdot e^{-2L/\ell_c}}{1 - R_2^2 \cdot e^{-4L/\ell_c}} \right). \tag{22}$$

In Fig. 11 the phase contrast is plotted as a function of the normalized thickness for different values of the reflection coefficient R_2. It is worth noting the following points:

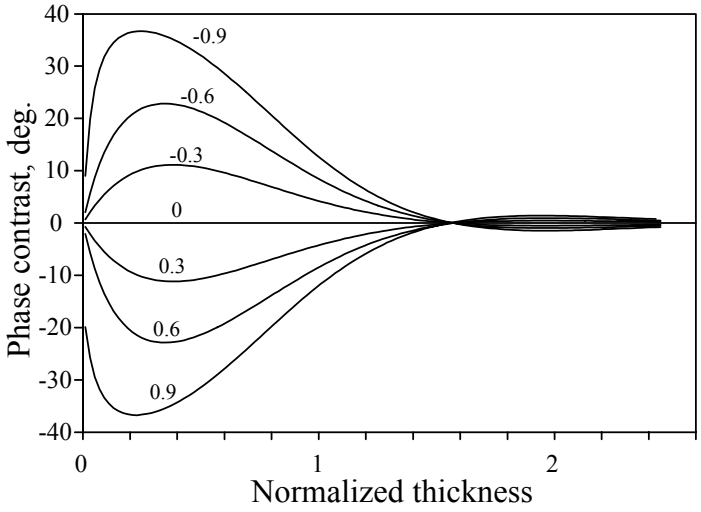

Fig. 11. Phase contrast $\Delta\phi$ vs the normalized thickness $L/\ell_C = L\sqrt{\pi f}/\sqrt{D_C}$ for different values of the reflection coefficient coating/bulk, according to Eq. (22).

(a) The phase contrast is subjected to the damped oscillations due to the interference; however only the first oscillation may be clearly seen and experimentally used. This happens when the coating thickness is not larger than the coating thermal diffusion length.
(b) The first oscillation of the phase contrast is positive for a negative value of R_2 and vice versa for symmetry. The oscillation increases with the absolute value of the reflection coefficient $|R_2|$ up to the limit $\Delta\phi=\pm 45°$ obtained for $R_2 = \mp 1$.

3.1 Thickness or thermal diffusivity measurements

The oscillation of the phase contrast may be exploited to measure the ratio $L/\sqrt{D_C}$ as well as the reflection coefficient R_2 [24,26]. In practice one measures the phase φ of the radiometric signal in a wide frequency range. At high frequency, the interference phenomenon becomes negligible, and the phase tends to a constant value that may be assumed as the reference phase φ_{ref}.

The phase contrast is thus obtained as $\Delta\phi=\varphi-\varphi_{ref}$. Finally the experimental $\Delta\phi$ should be compared with the theoretical one given by Eq.(22), frequency by frequency, where $L/\sqrt{D_C}$ and R_2 represent simply fit parameters.

As an example we applied this procedure on a single thin layer: a 200 μm thick Inox sample. In Fig. 12 the phase contrast $\Delta\phi$ is plotted as a function of $\sqrt{f}$; the square symbols represent the experimental data by photothermal radiometric technique, while the full lines represent the theoretical values, according to Eq. (22), where $L = 200\mu m$, $R_1 = R_2 = 1$, and the only fit parameter is therefore the Inox thermal diffusivity D_{Inox} which for the three curves is chosen to be 0.04, 0.046 or 0.06 cm^2/s. Simple inspection shows that the theoretical curve for $D_{Inox}=0.046\ cm^2/s$ fits very well the experimental data for $f>10Hz$. What happens for $f<10Hz$? For low frequencies, when the thermal diffusion length becomes comparable with the pump beam size, the geometry of the wavefront of the thermal waves, supposed to be plane, bends as happens for a spherical thermal wave. As a consequence the *1D model* (Eq. 5), which describes the temperature field as only *z*-dependent, becomes inadequate and should be replaced with a *3D model*.

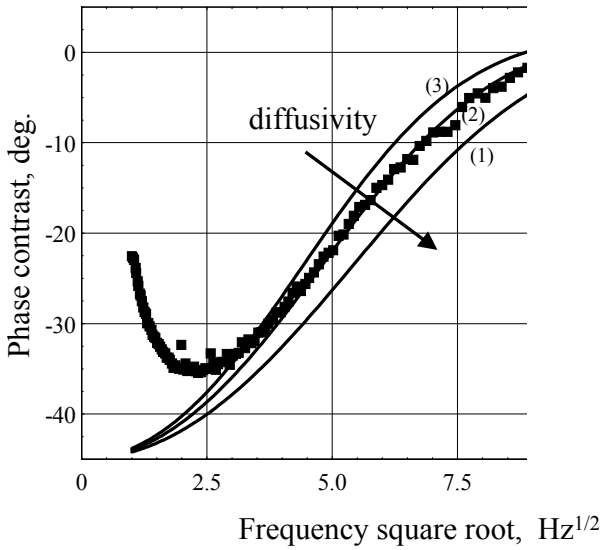

Fig. 12. Phase contrast $\Delta\phi$ vs the frequency square root: (■) experimental data for 200μm thick Inox sample; curves (1), (2) and (3) are obtained by Eq. (22) respectively for D_{Inox}=*0.06, 0.046*, and *0.04 cm²/s*.

In Fig. 13 we tried to fit even the data for *f<10Hz* by using a *3D model* which takes into account the Gaussian pump beam size *d* [15,27,28]. The full lines represent the theoretical values for different spot-sizes (*d = 1mm, 2.3mm, 5mm*), for the most probable diffusivity found in Fig. 12 (D_{Inox}=*0.046 cm²/s*); The curve for *d=2.3mm* fit now the data in the whole frequency range.

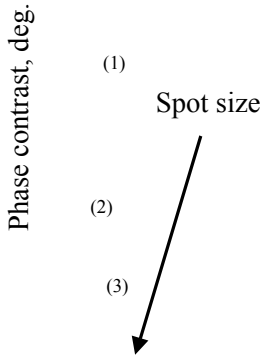

Fig. 13. Phase contrast $\Delta\phi$ vs the frequency square root: (■) experimental data for 200μm thick Inox sample; curves (1), (2) and (3) are obtained respectively for the pump spot sizes *d=1, 2.3, and 5 mm*. The diffusivity is kept to D_{Inox}=*0.046 cm²/s*.

Obviously in order to perform a systematic research of the best fit, we must report the standard deviation of the phase contrast (see Fig. 14) as a function of diffusivity (curve 1), and as a function of the spot-size (curve 2). Curve 1 allows to determine the most probable value of diffusivity together with its uncertainty D_{Inox}=*0.046 ± 0.005 cm²/s;* this value of diffusivity has been kept constant during the second fit (curve 2) which determines the most probable spot-size together with its uncertainty *d=2.3±0.4mm.*

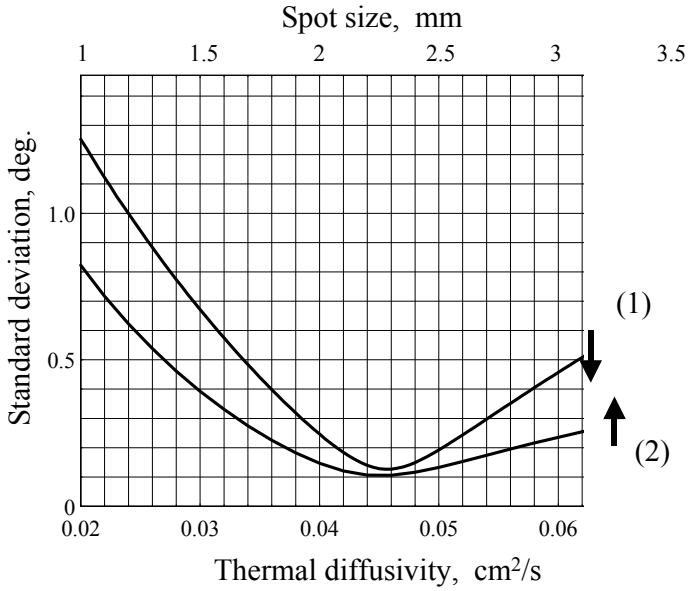

Fig. 14. Standard deviation of the phase contrast, for the data in Figs. 12 and 13.
curve 1: the standard deviation is plotted vs the Inox thermal diffusivity.
curve 2: the standard deviation is plotted vs the pump spot sizes for D_{Inox} *=0.046 cm²/s*.

Another procedure to determine $L/\sqrt{D_c}$ and R_2 uses the property of the so-called *thermal reflectivity* Γ defined as the ratio between the backward and the forward thermal wave (see *Thermal wave in layered materials*) [29]. In this case it is helpful to refer to the quantity $\sqrt{f}\cdot\hat{T}_{surf}(f)$, which has the main advantage to be non-vanishing at high frequency. According to Eq.(21), in fact, $\lim_{p\to\infty}\sqrt{p}\cdot\hat{T}_{surf}(p)=\frac{I}{(e_c+e_{air})\sqrt{2\pi j}}$, and consequently the *surface thermal reflectivity* Γ_{surf} may be expressed as a combination of the quantity $\sqrt{f}\cdot\hat{T}_{surf}(f)$ as follows [29,30]

$$\Gamma_{surf}=\frac{\sqrt{f}\cdot\hat{T}_{surf}(f)-\lim_{p\to\infty}\sqrt{p}\cdot\hat{T}_{surf}(p)}{\sqrt{f}\cdot\hat{T}_{surf}(f)+\lim_{p\to\infty}\sqrt{p}\cdot\hat{T}_{surf}(p)}=R_2\cdot\exp\left[-2(1+j)\frac{L\sqrt{\pi f}}{\sqrt{D_c}}\right]\Rightarrow\begin{cases}\ln\left(\left|\Gamma_{surf}\right|\right)=-2L\sqrt{\pi f}/\sqrt{D_c}+\ln[R_2]\\ \arg\left(\Gamma_{surf}\right)=-2L\sqrt{\pi f}/\sqrt{D_c}\end{cases}\quad(23)$$

Both the logarithm of amplitude and the phase of Γ_{surf}, when plotted as a function of $\sqrt{f}$, exhibit a linear behaviour with same linear slope $\left(-2\sqrt{\pi}\frac{L}{\sqrt{D_c}}\right)$ from which $L/\sqrt{D_c}$ is immediately worked out. The other parameter R_2 may be worked out by the difference $\ln\left|\Gamma_{surf}\right|-\arg\left(\Gamma_{surf}\right)=\ln[R_2]$. We have applied this procedure to the previous example of the 200μm thick Inox sample. In Fig. 15 both logarithm of amplitude and the phase of the *surface thermal reflectivity* are plotted vs $\sqrt{f}$. From the linear slope one obtains D_{Inox}*=0.049cm²/s* that is a little larger than the previous measurement; this small error is due to the finite spot-size which produces *3D effects* unpredicted by Eq.(23). Note also the small difference between the curves in Fig. 15. According to Eq. (23) this may be wrongly interpreted as if $R_2\neq 1$, but, on the opposite, once again it is due to the *3D effects*. This possible misunderstanding has deep roots in the general following consideration: on one side, the *3D* spherical effect due to the finite spot-size, reduces the efficiency of the thermal wave interference with respect to the plane case, and consequently limits the oscillation of $\Delta\phi$. If one refers to the theoretical curves

of Fig. 13, in which $R_1 = R_2 = 1$, it is evident that as the spot-size *d* decreases even the oscillation decreases.

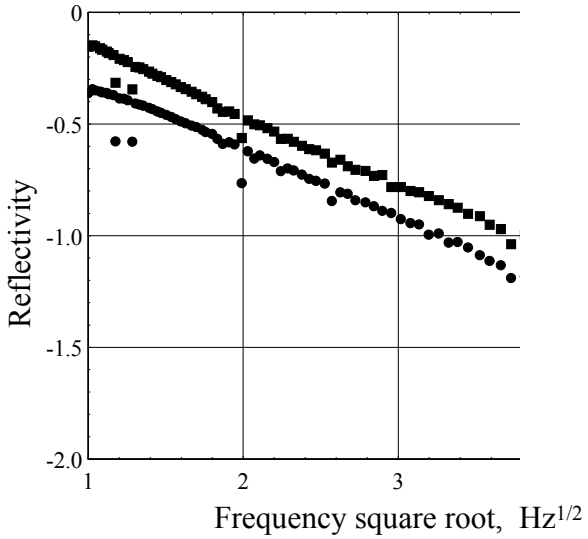

Fig. 15. The thermal reflectivity is plotted vs the frequency square root for the experimental data in Fig. 13. The symbols (■) represent the phase (radian) of the reflectivity; the symbols (●) represent the logarithm of the amplitude.

On the other side, even a non-perfect thermal reflection between coating and bulk $(R_2 \neq 1)$ is able to reduce the efficiency of the thermal wave interference with respect to the thermal wave mirror case $(R_2 = 1)$. This limits the oscillation of $\Delta\phi$ exactly as in the other case. The evidence is provided by the analogy between the curve for $R_2 = 0.6$ in Fig. 11, and the curve for *d=1mm* in Fig. 13. As a conclusion the interference efficiency is reduced due to thermal energy anyhow lost, whether in the lateral *x,y* direction for the spherical wave effect, or in the longitudinal *z* direction for the transmission in the bulk. Moreover, for simplicity, we haven't considered other secondary thermal energy losses, as for example the losses due to the heat convection in air or the infrared emission at the surface. Consequently the estimate of R_2 is a nontrivial task, when mainly the spot-size, but also the surface conductance, are not exactly known.

4. Thermal wave resonator

Although the thermal wave interferometry has been applied for long time in order to measure the thickness or the thermal diffusivity of solids, the *thermal-wave resonator* has been introduced only in 1995 [31]. Basically the physical process which takes place in a thin film periodically heated at one side is absolutely the same that occurs to a *thermal wave resonant cavity*: that is the interference between thermal waves propagating in opposite directions. One difference is the number of independent variables (*degrees of freedom*) available to observe the interference [32]. In other words if one applies the thermal wave interferometry to investigate the thermal thin film properties, the interference phenomena may be observed only by changing the frequency *f* of the periodical heating (i.e. thermal wavelength). In a *thermal wave resonant cavity* the number of degrees of freedom increases; in fact one may adjust the cavity length as well as the frequency *f* (i.e. thermal wavelength). Roughly speaking a plane thermal wave resonator is a cavity, whether open or closed, filled with air or any gas, delimited at least by two solid samples, with plane facets acting as thermal wave mirrors (see Fig. 16).

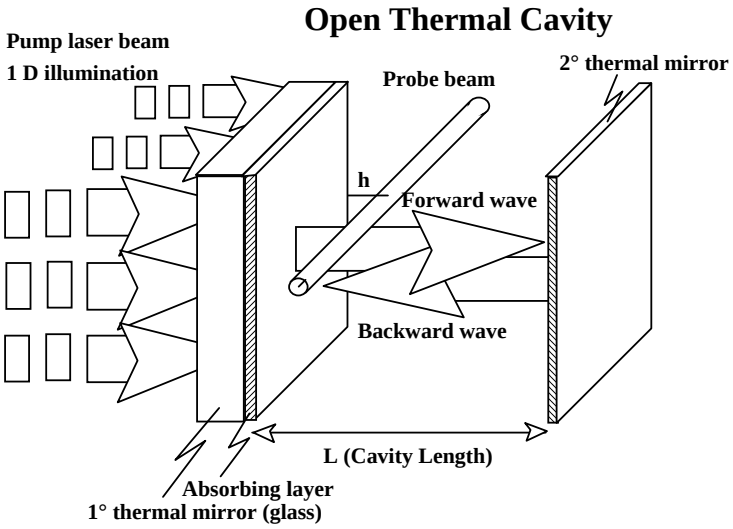

Fig. 16. Schematic representation of the plane thermal-wave resonator; the in situ photothermal deflection technique measures the gas thermal diffusivity.

In principle no special care should be required in the choice of the material for the thermal wave mirrors. In fact it has been already pointed out that any solid layer, even if extremely thin (see Fig. 3), naturally behaves as a thermal wave mirror with a thermal reflection coefficient $(R \approx -0.99)$ large enough to set-up the thermal wave resonator. On the contrary, in reality, a special care must be taken to build-up the first thermal wave mirror, which plays an active role in the thermal energy pumping. It is made of a thick glass slab coated by an optically opaque thin layer (see Fig. 16). In such a way a wide pump laser beam may pass through the glass, but is totally absorbed by the optically opaque thin layer. As a consequence the heat periodically induced in this layer generates plane thermal waves travelling in the cavity. Finally the thermal field in the cavity may be monitored by photothermal deflection technique, using a probe laser beam travelling in the gas at an adjustable distance from the active mirror.

4.1 General properties of a thermal wave resonator

In order to evaluate the properties of the resonator, we analyse some thermal features when the *thermal wave cavity* is working (*case a*), and when the second mirror is removed (*case b*). In particular we wish to compare the thermal field, the thermal energy, and the heat flux in the two cases. Concerning the thermal field in the gas for both cases one may write [32]

$$\begin{aligned} \hat{T}_{gas}(z) &= \frac{I}{e_1 \cdot \sqrt{j\omega}} \frac{(1+|R_1|)}{2} \frac{e^{-\beta_{air} z} - |R_2| e^{\beta_{air}(z-2L)}}{1-|R_1 R_2| e^{-2\beta_{air} L}} \quad 0 < z < L \quad case\ \ a) \\ \hat{T}_{gas}(z) &= \frac{I}{e_1 \cdot \sqrt{j\omega}} \frac{(1+|R_1|)}{2} e^{-\beta_{air} z} \qquad\qquad\qquad\qquad z > 0 \quad case\ \ b) \end{aligned} \tag{24}$$

where $|R_1| \approx |R_2| \approx 1$ are the absolute values of the thermal reflection coefficients of the two mirrors, e_1, e_2 the mirror' effusivity, L the cavity length, z the distance from the active mirror. Note that in *case b)*, the temperature simply decreases with z (distance from the source), while in *case a),* thermal wave interference takes place in the gas. We compare both thermal fields in three significant points: on the first mirror for $z=0$, in the cavity centre for $z=L/2$, and on the second mirror for $z=L$. The amplitude

ratio between *case a)* and *b)* vs the normalized cavity length L/ℓ_{gas} is plotted in Fig. 17, curve (a) for *z=0*, curve (b) for *z=L/2*, while for *z=L* the ratio is zero everywhere. It is worth nothing that:

(a) the temperature field on the first mirror is constant, has the same value as when the second mirror is absent and depends only on the heat directly deposited: therefore it is insensitive to the interference phenomenon.
(b) the temperature field on the second mirror is zero (destructive interference) because there is no direct heat deposition, and, moreover, the thermal wave in the gas is nor able to heat the mirror (no relevant transmission).
(c) the temperature field in the cavity centre changes by varying the cavity length which is a typical effect of interference, but there is not any relevant thermal gain to justify the use of a resonator for this scope.

Another fundamental feature to be analysed is the thermal energy stored in the gas, which obviously oscillates at the same frequency of the temperature. This quantity may be defined as $\hat{E}_{gas} = \int_{V_{gas}} (\rho c)_{gas} \cdot \hat{T}_{gas} dV$ and may be calculated for the temperature in Eq. (24) as follows

$$\begin{aligned} \hat{E}_{gas} &= \frac{P}{j\omega} \frac{1-|R_1|}{2} \frac{\left(1-|R_2|e^{-\beta_{gas}L}\right)\left(1-e^{-\beta_{gas}L}\right)}{1-|R_1R_2|e^{-2\beta_{gas}L}} \qquad case\ \ a) \\ \hat{E}_{gas} &= \frac{P}{j\omega} \frac{1-|R_1|}{2} \qquad case\ \ b) \end{aligned} \tag{25}$$

It is worth noting that, in both *cases a)* and *b)*, the energy stored in the gas is extremely small with respect to the total available energy that is $P/j\omega$. For example, in *case b)*, the fraction of energy in the gas is $(1-|R_1|)/2 < 0.5\%$. Why? The physical reason is due to the extremely low gas heat capacity, so that even if the gas temperature is relevant (see Eq. 24), there is no significant energy. Where is the remaining 99.5% of energy? In the heated solid (active mirror). Although $\hat{E}_{gas}$ is very low, one may compare the gas energy in *cases a)* and *b)*, by plotting their energy ratio vs the normalized cavity length L/ℓ_{gas} (see curve (c) in Fig. 17). The amplitude ratio is always smaller than *1.2*, from which one deduces that the use of the thermal wave cavity does not allow any relevant increase of the energy level in the gas.

Last fundamental feature to be analysed is the heat flux. A good estimate of such a quantity is provided by the photothermal deflection angle, which is proportional to both the thermal gradient and the heat flux, as already pointed out in Eq. (12). By combining Eqs. (12) and (24) one obtains for the deflection angle in the two cases

$$\begin{aligned} \hat{\Phi}_z(z) &= \left(\frac{-1}{n_{gas}}\frac{dn_{gas}}{dT}\frac{1+|R_1|}{2}\sqrt{\frac{D_1}{D_{gas}}}\frac{I}{k_1}L_{eff}\right)\cdot\frac{e^{-\beta_{air}z}+|R_2|e^{\beta_{air}(z-2L)}}{1-|R_1R_2|e^{-2\beta_{air}L}} \quad 0<z<L \qquad (a) \\ \hat{\Phi}_z(z) &= \left(\frac{-1}{n_{gas}}\frac{dn_{gas}}{dT}\frac{1+|R_1|}{2}\sqrt{\frac{D_1}{D_{gas}}}\frac{I}{k_1}L_{eff}\right)\cdot e^{-\beta_{air}z} \qquad z>0 \qquad (b) \end{aligned} \tag{26}$$

As usual we may compare the deflection angle in *case a)* and in *case b)*, in three significant points of the resonator: on the first mirror for *z=0*, in the cavity centre for *z=L/2,* and on the second mirror for *z=L*. The amplitude ratio vs the normalized cavity length L/ℓ_{gas} is plotted in Fig. 17, curve (d) for *z=0*, curve (e) for *z=L/2*, curve (f) for *z=L*. The ratio of the heat fluxes or of the thermal gradients, for the two *cases a)* and *b)* gives exactly the same results as the amplitude ratio for deflections, which thus has general validity. By a first inspection of curves *d,e,f*, one may see that the amplitude ratio may reach very high values for a short cavity. In fact if $z, L \to 0$, the amplitude ratio tends to the

value $2/(1-|R_1R_2|)$ which may be extremely high. As a conclusion, in a short thermal wave cavity, the heat flux, the thermal gradients and the beam deflection are magnified and amplified with respect to the standard case. There are at least two physical explanations for this:

(a) it has been shown that the temperature on the active mirror is constant, let's say T_1, while the temperature on the second mirror is kept to zero. Therefore the effective thermal gradient is $dT/dz = T_1/L$ which may become a huge value if $L \to 0$.

(b) Generally on a mirror there is a destructive interference for the temperature, but a constructive interference for the thermal gradient. In other words the use of one mirror doubles the existing (incident) thermal gradient. The use of two mirrors, at short distance, may reinforce farther the thermal gradient.

As a conclusive remark the use of a thermal wave resonator may amplify any quantity related to the thermal gradient; in particular the use of a thermal wave resonator may increase the sensitivity of the photothermal deflection technique in the measurements of the thermal diffusivity of gases, due to the signal amplification. In principle the gain of such a device could be very high $2/(1-|R_1R_2|)$. Unfortunately in reality the gain is limited by the 3D spherical effect related to the pump beam finite spot-size *a*. In fact the spherical thermal waves produced on the first mirror, propagates not only along the cavity but also in undesired directions out of cavity. This reduces the thermal wave interference pattern and causes the loss of the ideal amplification. In practice values of 10-20db may be easily obtained.

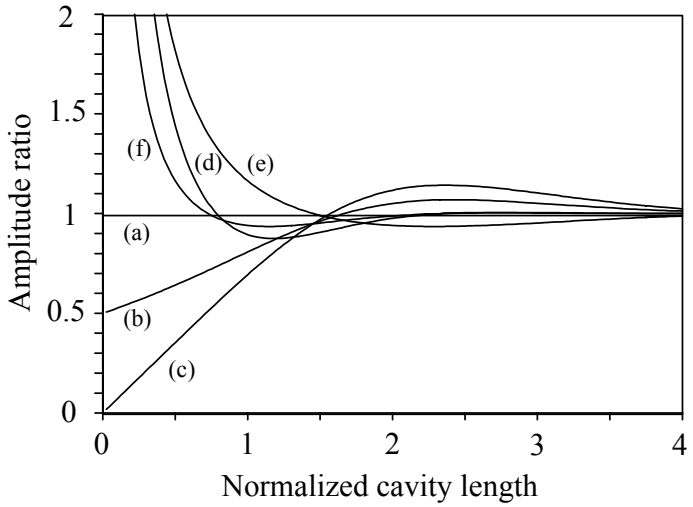

Fig. 17. The thermal properties in the cavity and without the cavity are compared. The ratio between *case a)* and *case b)* is plotted vs $L/\ell_{gas} = L\sqrt{\pi f / D_{gas}}$ (*normalized cavity length*) for temperature, thermal energy, and deflection: curves (a), (b) are the temperature ratios on the first mirror and in the cavity centre; curve (c) is the thermal energy ratio, curves (d),(e) and

(f) are the deflection ratios respectively for *z=0, z=L/2, z=L*.

4.2 Experimental evidences on the thermal wave resonator

Let us consider a plane thermal wave open resonator in which the active mirror is a thick glass layer coated by a thin pump-absorbing film (1μm Silicon), and the second plane mirror is a 20 μm thick aluminium foil. In the open cavity there is air in standard conditions of pressure and temperature. The pump beam is a 250 mW Ar laser, heating the thin silicon film with a 1 mm spot-size. The cavity length may be adjusted from 0.1mm to 2mm, by moving the second mirror. The mechanical chopper may adjust the working frequency in the range 1-1500 Hz. The probe beam is coming from a 633 nm He-Ne laser. The beam travels in *x* direction, at a adjustable distance *z* from

the active mirror, and is deflected in the *z* direction. Its probe beam deflection is detected by a position sensor, and processed by a lock-in amplifier.

An experimental evidence of the thermal wave interference effect in air is given in Fig. 18 where the phase of the deflection signal is plotted vs the frequency square root (i.e. the normalized cavity length $L\sqrt{\pi f}\,/\sqrt{D_{air}}$) for three different probe beam positions in the cavity ($z \approx 0$, $z=L/2$ and $z \approx L$) (*case a*). In the same figure for comparison, the measurement has been repeated for $z \approx 0$, removing the second mirror (*case b*). The effect of the thermal wave resonator is clearly seen in the differences between *case a* (■) and *case b* (+). It is worth noting that the difference exist only for $f<25Hz$ because:

(a) if $f<25Hz$ the thermal waves induced on the first mirror have a long thermal wavelength. These long waves are subjected to a weak attenuation, but are able to reach the second mirror, "*feel*" if the mirror is removed or not. Consequently take part, or not to the interference in the cavity.

(b) If $f>25Hz$ the induced thermal waves have a short thermal wavelength. In this case they are subjected to a large attenuation, do not reach the second mirror, and cannot anyway interfere in the cavity, in case there is a cavity! In this regime the difference between *case a)* and *case b)* is only potential.

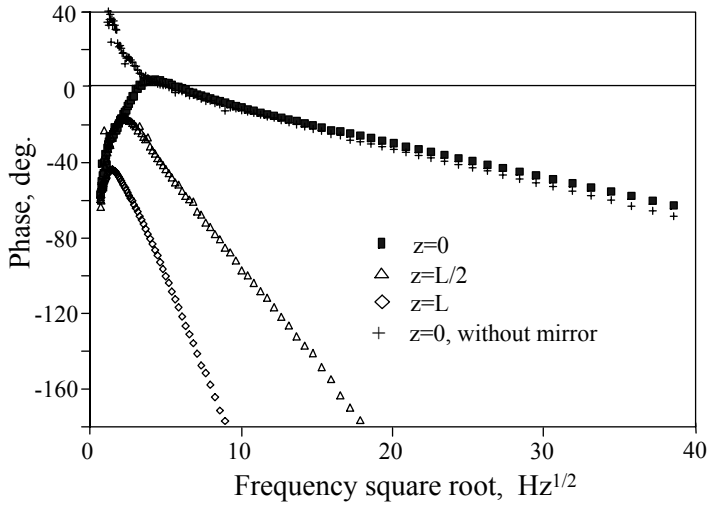

Fig. 18. Phase (radian) of the deflection signal vs the frequency square root ($Hz^{1/2}$) measured in different points: (■) for z=0, (Δ) for z=L/2, (◊) for z=L, (+) for z=0 without cavity.

4.3 Gas thermal diffusivity measurements

In order to increase the sensitivity of the photothermal deflection technique for thermal diffusivity measurements of non-absorbing gases, one may exploit the deflection amplification effect in a thermal wave resonator [32,33]. As one may see from the expression of the photothermal signal (see Eq. 26a), there are three free parameters to be adjusted: the cavity length *L*, the probe beam position *z*, and the frequency *f* (i.e. ℓ_{gas}). Therefore one may perform the measurements keeping constant two parameters, and varying the third one. In principle one may choose one of the following three procedures: a cavity length scan, a probe beam scan, or a frequency scan. In all cases is possible to see the interference effect in the resonator, and to measure the gas thermal diffusivity by fitting the data with the theory.

As an example we applied the cavity length scan method to measure the air thermal diffusivity in an open thermal wave resonator. In Fig. 19 both logarithm of amplitude and phase are plotted vs the cavity length in the range from 100μm to than 1400 μm. The other two parameters are kept constant: the probe beam has been placed at 70μm from the first mirror and the mechanical chopper frequency worked at f = 36Hz. Note the typical oscillation of both phase and amplitude due

to the thermal wave interference. Note also that for short cavity length there is an amplitude amplification larger than 10db. From the fit with the theory, one obtains the value $D_{air} = 0.205 \ \ cm^2 / s$. Instead of such nonlinear fit for phase and amplitude, one may perform an easier linear fit for *thermal reflectivity* (see Eq. 23*)*. In fact, the deflection in Eq.(26a), can be seen as the sum of two terms which refer to the forward and backward plane thermal waves. It is well know that the ratio between the backward and the forward wave, called *thermal reflectivity*, has an easy single-exponential expression useful for linear fit. But is it possible, starting from the sum of the two quantities mixed together in Eq.(26a) to calculate its ratio? The answer is positive only if an additional information is provided, as for example the value of the forward wave when the backward is absent, for instance when the cavity length L tends to infinity. It is easy to demonstrate that the thermal reflectivity Γ may be obtained as follows [32]

$$\Gamma(L) = \frac{\hat{\Phi}_z(L) - \hat{\Phi}_z(\infty)}{\hat{\Phi}_z(L) + \hat{\Phi}_z(\infty)} = \frac{R_2(1+R_1)}{2} \exp\left[-2(1+j)(L-z)/\ell_{gas}\right] =$$
$$= \begin{cases} \ln(|\Gamma|) = -2(L-z)/\ell_{gas} + \ln\left[R_2(1+R_1)/2\right] \\ \arg(\Gamma) = -2(L-z)/\ell_{gas} \end{cases} \tag{27}$$

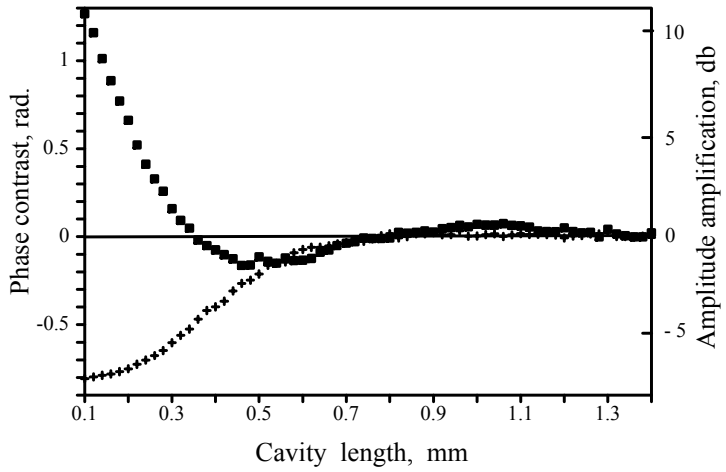

Fig. 19. Deflection signal as a function of the cavity length L (mm). The frequency is fixed to f=36Hz, The spot size is 1mm wide. The thermal wave resonator works in air: (■) Logarithm of amplitude (db), (+) phase contrast (radian).

Note that both the logarithm of amplitude and the phase of the reflection coefficient have the same linear behaviour in the three variables L, z $\sqrt{f}$. By the linear slopes of both phase and logarithm of amplitude of Γ, the diffusivity can be worked out by one of the two relationships

$$D_{gas} = 4\pi f \left(N_L \Big/ \frac{\Delta \ln(|\Gamma|)}{\Delta L} \right)^2$$
$$D_{gas} = 4\pi f \left(N_L \Big/ \frac{\Delta \arg(\Gamma)}{\Delta L} \right)^2 \tag{28}$$

where the corrective factor N_L has also been introduced, to take into account the 3D spherical effect due to the spot-size a. In Fig. 20 the results of a numerical study on the factor N_L is presented.

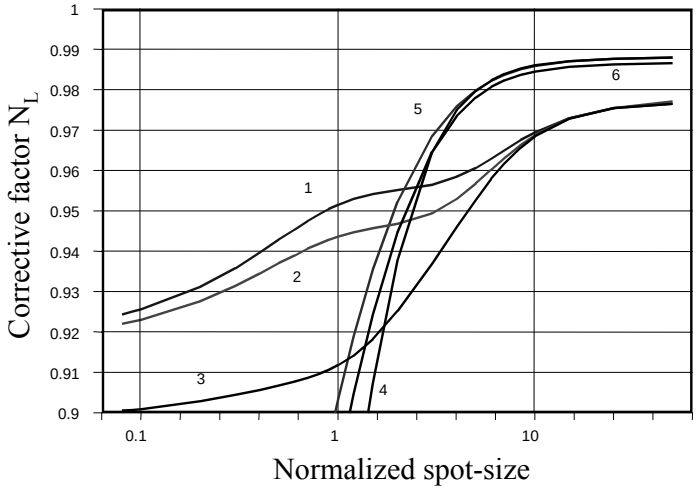

Fig. 20. Numerical analysis of the factor N_L , due to the finite spot size of the pump beam. In abscissa is a/ℓ_{gas} . The curves refer to different formula (phase and amplitude) and to different thermal diffusivity between gas and sample D_{ratio}: amplitude formula; (curve 1) D_{ratio}=0.2; (curve 2) D_{ratio}=0.5; (curve 3) D_{ratio}= 5; phase formula; (curve 4) D_{ratio}= 0.2; (curve 5) D_{ratio}=0.5; (curve 6) D_{ratio}=5.

The N_L values for both amplitude and phase formula are plotted as a function of the parameter a/ℓ_{gas} , for different diffusivity ratios between gas and active mirror D_{gas}/D_1 (0.2 - 0.5 - 5). For large a/ℓ_{gas} all the curves tend to 1, but in a different way, so that the amplitude formula in Eq.(28a) is normally preferred. From a experimental point of view we calculate the thermal reflectivity from the data in Fig. 19, by using Eq.(27) and taking for $\hat{\Phi}_z(\infty)$ the $\hat{\Phi}_z$ value obtained for the longest cavity length (0.14mm). In fact this distance is enough to inhibit the thermal waves from doing a complete round trip in the resonator. In Fig. 21 both phase and logarithm of amplitude of Γ are plotted vs the cavity length L. The expected linear behaviour is present for the first 500 μm. For larger distances the interference between the damped forward and backward waves becomes ineffective. Looking at the linear slopes and using Eqs.(28) one may calculate the air thermal diffusivity.

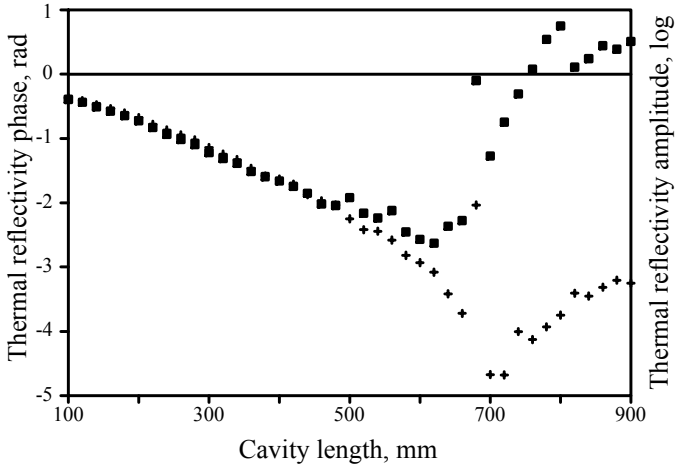

Fig. 21. Thermal reflectivity vs the cavity length L (mm) : (■) phase contrast (radian); (+)

logarithm of amplitude.

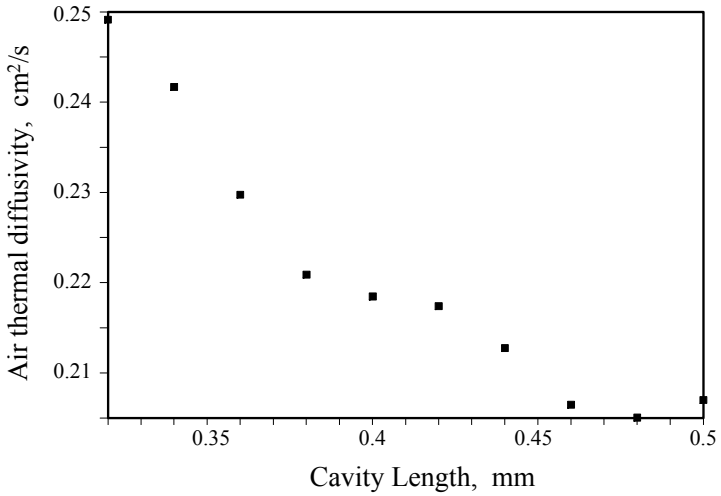

Fig. 22. Air thermal diffusivity vs the cavity length L (mm).

In this case a small distortion from linearity occurs to both phase and logarithm of amplitude. This effect can be related to a variable value of the air diffusivity. In fact with 250mW pump beam power, by changing the cavity length of the resonator the d.c. temperature rise inside it, could reach several tens of degree which are able to increase the air thermal diffusivity of several percents. By applying Eqs.(28) locally, one obtains the calculated profile of air thermal diffusivity as a function of the cavity length (see Fig. 22). For cavity lengths larger than 450μm the effect of the d.c. temperature rise seems negligible so that the diffusivity decreases to the standard value of about 0.205 cm^2/s at the room temperature of 20 C [18].

5. Thermal waves in layered materials

In this section we only want to provide some useful tool to solve the heat conduction equation in periodical regime for layered materials [29,30,34-40]. One basic problem, as previously discussed in thermal wave interferometry, is to find a suitable algorithm to calculate the thermal field in a layered material periodically heated at the surface, assuming to know the thickness, the thermal effusivity and the thermal diffusivity of each layer [29,41-43]. In the generic i^{th} layer the temperature field may be written as the superposition of a forward and a backward plane thermal wave as follows [29,30]

$$\hat{T}_i(z) = A_i \cdot \exp[-\beta_i z] + B_i \cdot \exp[\beta_i z], \tag{29}$$

where $\beta_i = \sqrt{j\omega/D_i}$ and D_i respectively are the wavevector and the thermal diffusivity of the i^{th} layer, and A_i , B_i are the unknown quantities to be determined from the boundary conditions (see Eq. 6). In practice there are 2 equations at each interface between two different layers, because both temperature and heat flux must be continuous functions. In case of N layers one has to solve a linear system of $2N$ equations (boundary conditions) and $2N$ unknown quantities (A and B for each layer) by the means of the usual algebraic methods. An alternative faster method uses the *thermal reflectivity*, defined as the ratio between the backward and the forward plane thermal waves in the i^{th} layer as follows $\Gamma_i(z) = B_i/A_i \ \exp[2\beta_i z]$. This method is recursive and allows one to calculate Γ, layer by layer starting from the last, back to the first, as it will be clear later. The procedure is based on the four following steps:

1- Description of the thermal reflectivity discontinuity at the interface $z=z_i$ between the i^{th} and $(i+1)^{th}$ media. The boundary conditions for $\widetilde{T}, \widetilde{F}$ may be written as follows [29,30]

$$\begin{cases} A_i \ \exp[-\beta_i z] \ [1+\Gamma_i(z_i)] = A_{i+1} \ \exp[-\beta_{i+1} z_i] \ [1+\Gamma_{i+1}(z_i)] \\ e_i\sqrt{j\omega} \ A_i \ \exp[-\beta_i z] \ [1-\Gamma_i(z_i)] = e_{i+1}\sqrt{j\omega} \ A_{i+1} \ \exp[-\beta_{i+1} z_i] \ [1-\Gamma_{i+1}(z_i)] \end{cases}. \quad (30)$$

By dividing the two expressions in Eq.(30) one for the other, one obtains

$$\frac{e_i}{e_{i+1}} \frac{1-\Gamma_i(z_i)}{1+\Gamma_i(z_i)} = \frac{1-\Gamma_{i+1}(z_i)}{1+\Gamma_{i+1}(z_i)}, \quad (31)$$

and after some algebra one finally finds the useful relationship

$$\Gamma_i(z_i) = \frac{r_{i,i+1} + \Gamma_{i+1}(z_i)}{1 + r_{i,i+1} \cdot \Gamma_{i+1}(z_i)} \quad (32)$$

where $r_{i,i+1} = \frac{e_i - e_{i+1}}{e_i + e_{i+1}}$ is the interface thermal reflection coefficient (see Eq.9).

2- Description of the thermal reflectivity attenuation inside the i^{th} layer. The thermal reflectivity, in this case, is a continuous function of *z*, subjected to a double exponential decay with respect to the thermal wave's one. In particular if the value $\Gamma_i(z_i)$ at the interface $z=z_i$ is known, the value $\Gamma_i(z_{i-1})$ at the other interface $z=z_{i-1}$ may be easily calculated as follows

$$\Gamma_i(z_{i-1}) = \Gamma_i(z_i) \cdot \exp[-2\beta_i(z_i - z_{i-1})]. \quad (33)$$

3- Description of the initial condition at infinity. The last layer (usually air) is supposed to be semi-infinite, so that the thermal reflectivity is everywhere

$$\Gamma_N(\infty) = \Gamma_N(z_{N-1}) = 0, \quad (34)$$

because there is not any backward wave.

4- Description of the surface condition.

The value of the thermal reflectivity in the first layer $\Gamma_{surf} = \Gamma(0)$ is strictly related to the surface temperature, by the heat flux condition at $z = 0$ as follows

$$\begin{aligned} -k_{air}\frac{d\hat{T}_{air}}{dz} + I &= -k_1\frac{d\hat{T}_1}{dz} \\ k_1\beta_1 A_1(1-\Gamma_{surf}) + k_{air}\beta_{air}A_1(1+\Gamma_{surf}) &= I \end{aligned} \quad (35)$$

and after some algebra

$$\hat{T}_{surf} = \frac{I}{e_1\sqrt{j\omega}} \frac{1+r_{1,air}}{2} \frac{1+\Gamma_{surf}}{1-\Gamma_{surf} \cdot r_{1,air}} \approx \frac{I}{e_1\sqrt{j\omega}} \frac{1+\Gamma_{surf}}{1-\Gamma_{surf}}, \quad (36)$$

where one may assume $r_{1,air} \approx 1$ for the reflection coefficient between air and the surface. In synthesis, if one starts from Eq. (34), combining iteratively Eqs. (32) and (33), finding the surface thermal reflectivity, by using Eq. (36) the surface temperature is eventually determined.

6. Thermal wave back scattering

In this section a new method is developed to describe the 1D heat diffusion process in inhomogeneous materials with thermal conductivity *k(z)* and heat capacity $\rho c(z)$ both functions of depth. In such a case the Fourier heat diffusion equation (1) becomes

$$\frac{\partial}{\partial z}\left[k(z)\frac{\partial \hat{T}(z)}{\partial z}\right] - j\omega\rho c(z)\hat{T}(z) = 0 \quad , \qquad (z>0) \tag{37}$$

being *T* independent on *x*,*y*. By introducing the heat flux, Eq.(37) may be written as a pair of coupled first order differential equations as follows [44,45]

$$\begin{cases} \hat{F}(z) = -k(z)\dfrac{\partial \hat{T}(z)}{\partial z} \\ \dfrac{\partial \hat{F}(z,t)}{\partial z} = -j\omega\rho c(z)\hat{T}(z) \end{cases} \tag{38}$$

subjected to the boundary condition at the surface $\hat{F}(0) \approx I$ (see Eq.35). For a homogeneous layer the solution of Eq. (38) may be expressed as a superposition of a forward exponential term and a backward one, as follows

$$\begin{cases} \hat{T}_i(z) = A_i \cdot \exp[-\beta_i z] + B_i \cdot \exp[\beta_i z] \\ \hat{F}_i(z) = e_i\sqrt{j\omega}\{A_i \cdot \exp[-\beta_i z] - B_i \cdot \exp[\beta_i z]\} \end{cases} \tag{39}$$

It is worth noting that both quantities $\widetilde{T}, \widetilde{F}$ have similar expressions; the only differences are in the opposite sign of the backward term and in the factor $\{e(z)\sqrt{j\omega}\}$. In fact the sign of the heat flux contains the information on the directionality of the thermal wave, that is clearly opposite for the forward and backward terms, while the factor $\{e(z)\sqrt{j\omega}\}$ represents the ratio between heat flux and temperature for a single thermal wave, and depends only on the effusive property of the layer. The question is now: how is it possible to extend these considerations to an inhomogeneous sample? Indeed an inhomogeneous sample, described by the quantities *k(z)* and *D(z)* both function of depth, may be modelled as a stack of homogeneous thin layers. Obviously in each layer Eq. (39) is still valid, with the appropriate *A* and *B* to be found. Since *A* and *B* depend on the specific layer, they may be considered complicate functions of depth. This consideration legitimates to search the solution of Eq. (38) in the following form

$$\begin{cases} \widetilde{T}(z) = \widetilde{T}_f(z) + \widetilde{T}_b(z) \\ \widetilde{F}(z) = e(z)\sqrt{j\omega}\ \left[\widetilde{T}_f(z) - \widetilde{T}_b(z)\right] \end{cases} \tag{40}$$

where $\widetilde{T}_f$ and $\widetilde{T}_b$ respectively are the forward and the backward fields, and represent the generalisation of Eq. (39). Obviously the proposed solutions in Eq. (40) must fulfil the condition in Eq. (38), which gives rise to the following first order coupled differential equation system [44,45]

$$\begin{cases} \dfrac{d\widetilde{T}_f}{dz}+\dfrac{d\widetilde{T}_b}{dz}=-\sqrt{\dfrac{j\omega}{D(z)}}\left[\widetilde{T}_f-\widetilde{T}_b\right] \\ \dfrac{d\widetilde{T}_f}{dz}-\dfrac{d\widetilde{T}_b}{dz}=-\sqrt{\dfrac{j\omega}{D(z)}}\left[\widetilde{T}_f+\widetilde{T}_b\right]-\dfrac{de}{dz}\dfrac{1}{e(z)}\left[\widetilde{T}_f-\widetilde{T}_b\right] \end{cases} \tag{41}$$

and after some algebra

$$\begin{cases} \dfrac{d\widetilde{T}_f}{dz}=-\sqrt{\dfrac{j\omega}{D(z)}}\ \widetilde{T}_f-\dfrac{1}{2}\dfrac{d\ln[e(z)]}{dz}\left[\widetilde{T}_f-\widetilde{T}_b\right] \\ \dfrac{d\widetilde{T}_b}{dz}=\sqrt{\dfrac{j\omega}{D(z)}}\ \widetilde{T}_b+\dfrac{1}{2}\dfrac{d\ln[e(z)]}{dz}\left[\widetilde{T}_f-\widetilde{T}_b\right] \end{cases} \tag{42}$$

The system Eqs. (42) is still coupled and difficult to be solved. A fundamental simplification comes when the thermal reflectivity Γ is introduced as the ratio between the backward and the forward fields $\Gamma=\widetilde{T}_b/\widetilde{T}_f$. The first derivative of Γ may be written as

$$\frac{d\Gamma}{dz}=\frac{d\widetilde{T}_b}{dz}\frac{1}{\widetilde{T}_f}-\frac{d\widetilde{T}_f}{dz}\frac{\Gamma}{\widetilde{T}_f} \tag{43}$$

which combined with Eq.(43), may be written as follows [30,44,45]

$$\frac{d\Gamma}{dz}=2\sqrt{\frac{j\omega}{D(z)}}\ \Gamma+\frac{1}{2}\frac{d\ln[e(z)]}{dz}\left[1-\Gamma^2\right] \tag{44}$$

subjected to the boundary condition to infinity,

$$\lim_{z\to\infty}\Gamma(z)=0\,, \tag{45}$$

and the final condition at the surface

$$\widetilde{T}_{surf}=\frac{I}{e_{surf}\sqrt{j\omega}}\frac{1+\Gamma(0)}{1-\Gamma(0)}. \tag{46}$$

By a first inspection, Eq.(44) is a first order nonlinear differential Riccati-type equation, which may be solved more easily than the second order differential Fourier Eq.(37). As a conclusion Eqs. (44),(45) and (46), found without any approximation, suggest an easy procedure to calculate the surface temperature. But the main problem is that, in the general case, Eq.(44) has no analytical solution and should be computed by using the standard numerical methods. However in many cases, the sample exhibits a slowly varying effusivity profile *e(z)*, which is limited in a range $e_{\min}<e(z)<e_{\max}$. In such a case, if the range is not too large, the amplitude of the thermal reflectivity Γ is much smaller than 1, and the nonlinear term Γ^2 in Eq. (44) may be neglected (Rayleigh approximation); the validation of the previous approximation may be given by the condition $|\Gamma(z,f)|\le\dfrac{\ln[e_{\max}/e_{\min}]}{2}$«1, which provides a strong criterion to establish the limit of validity of the following model. The suppression of the nonlinear term in Eq. (44) leads to a first-order linear differential equation whose solution may be always put in a close form as follows [30,44,45]

$$\Gamma(0,f)=\int_0^\infty\frac{-d\ln(e(z))}{2dz}\exp\left[-2(1+j)\sqrt{\pi f}\int_0^z\frac{d\delta}{\sqrt{D(\delta)}}\right]dz \tag{47}$$

Before going on, it is worth to notice that Eq.(47) has a clear physical meaning. The thermal wave is generated by a laser at the surface, then it propagates along *z*, and is partially reflected back when finds some effusivity inhomogeneity which acts exactly as backscattering centre. The total amount of the thermal wave reflected back is therefore given by the integral over the whole volume (*dz*) of all the back-scattering contributions. Eq.(47) is in fact a back-scattering integral where the logarithmic term plays the role of the source for the scattering field, while the exponential term represents the attenuation of a thermal wave travelling two times the distance between the surface and the scattering centre at the depth *z* (one trip to reach the inhomogeneity, plus one trip back to the surface after reflection): note that the *thermal wave round trip* occurs in a inhomogeneous medium, as taken into account in the diffusivity integral inside the bracket. According to this explanation the heat diffusion model based on Eq.(47) may be reasonably called *thermal wave back-scattering* theory (TWBS).

Now the question is "which is the range of validity of TWBS?". In order to test the validity of the thermal wave scattering model, one may compare the surface temperature obtained by Eqs.(46) and (47), with the exact solution, for a significant type of profile [46-50]. As an example we refer to the linear conductivity depth profile for which an exact solution exists, if the heat capacity is constant. The inhomogeneous specimen under test is therefore given by the following conductivity profile [46,47]

$$\begin{cases} k(z) = k_{surf} + \left(k_{bulk} - k_{surf}\right) z/L & 0 < z < L \\ k(z) = k_{bulk} & z > L \end{cases} \tag{48}$$

where L is the size of the inhomogeneous behaviour, and k_{surf} , k_{bulk} are the conductivity values for $z=0$ and for $z>L$. Obviously a useful parameterization is requested to eliminate some unessential parameters. In analogy with the thermal wave interferometry (see Fig. 11) we refer to the only independent quantities: the normalized thickness $L/\ell_{bulk} = L\sqrt{\pi f}\,/\sqrt{D_{bulk}}$, and the effective thermal reflection of the structure $R = \dfrac{e_{surf} - e_{bulk}}{e_{surf} + e_{bulk}} = \dfrac{\sqrt{k_{surf}} - \sqrt{k_{bulk}}}{\sqrt{k_{surf}} + \sqrt{k_{bulk}}}$. In Fig. 23 the phase contrast for surface temperature is plotted vs the normalized thickness for different values of *R*. The curves 1,2,3 represent the exact solution for *R=0.2, 0.4, 0.6*, while curves 4,5,6 correspond to the thermal wave backscattering solution (*TWBS solution*). It is worth noting that:

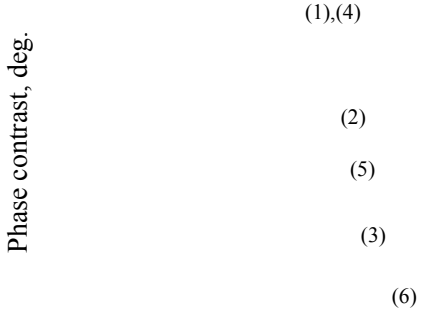

Fig. 23. Phase contrast vs the normalized thickness $\left(L/\ell_{bulk} = L\sqrt{\pi f}\,/\sqrt{D_{bulk}}\right)$ for the linear conductivity profiles in Eq.(48): curves (1),(2),and (3) are the exact solution for *R = 0.2, 0.4, 0.6;* curves (4), (5), and (6) are the *TWBS solution* for *R=0.2, 0.4, 0.6.*

(a) the phase contrast exhibits one oscillation only, instead of the damped oscillations of the two-layers system (see Fig.11). Such oscillation happens when $L \approx \ell_{bulk}$ and increases with the effective thermal reflection *R*, just a little less with respect to the two-layers system. This means that the thermal wave backscattering is less efficient than the thermal wave reflection.

(b) The difference between the exact solution and the TWBS solution is seen only for high values *R*, when the nonlinear term in the Riccati Eq.(47) cannot be neglected without a remarkable error.

In Fig. 24 the absolute value of the error of the TWBS solution is plotted vs the normalized thickness for the standard values of *R* (curves 1,2,3 correspond to *R=0.2, 0.4, 0.6*). The error has a maximum in the low frequency regime, which may be predicted by the theory considering that $\lim_{f\to 0}\Gamma(f) = \frac{1}{2}\ln\left(\frac{e_{surf}}{e_{bulk}}\right) = \frac{1}{4}\ln\left(\frac{k_{surf}}{k_{bulk}}\right)$, so to obtain the following analytical expression for the maximum value of the error

$$\lim_{f\to 0} error = \left| \frac{\dfrac{I}{e_{surf}\sqrt{j\omega}}\dfrac{1+\Gamma(0,f)}{1-\Gamma(0,f)}}{\dfrac{I}{e_{bulk}\sqrt{j\omega}}} - 1 \right| = \left| \frac{1-R}{1+R}\cdot\frac{2+\ln\left(\dfrac{1+R}{1-R}\right)}{2-\ln\left(\dfrac{1+R}{1-R}\right)} - 1 \right| \tag{49}$$

which is plotted as a function of *R,* in fig.25. Of course this is the error in the worse case at very low frequency and the validity of TWBS solution in the whole frequency spectrum is much wider. As a conclusive remark, although TWBS is an approximated model, it is very useful because it establishes a clear relationship between effusivity profile *e(z),* diffusivity profile *D(z)* and surface thermal reflectivity $\Gamma(0, f)$. Such simple relationship may be used to solve a typical inverse problem called *photothermal depth profiling* which consists in the retrieval of the diffusivity profile *D(z)* in inhomogeneous materials, as described in the next paragraph.

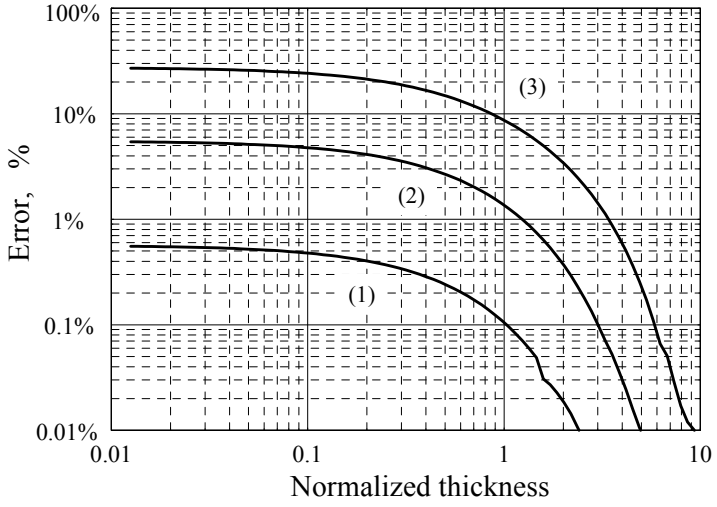

Fig. 24. Error between *TWBS* and exact solutions vs the normalized thickness thickness $\left(L/\ell_{bulk} = L\sqrt{\pi f}\,/\sqrt{D_{bulk}}\right)$ for the linear conductivity profiles in Eq.(48): curve (1) *R=0.2;*

curve (2) *R=0.4;* curve (3) *R=0.6.*

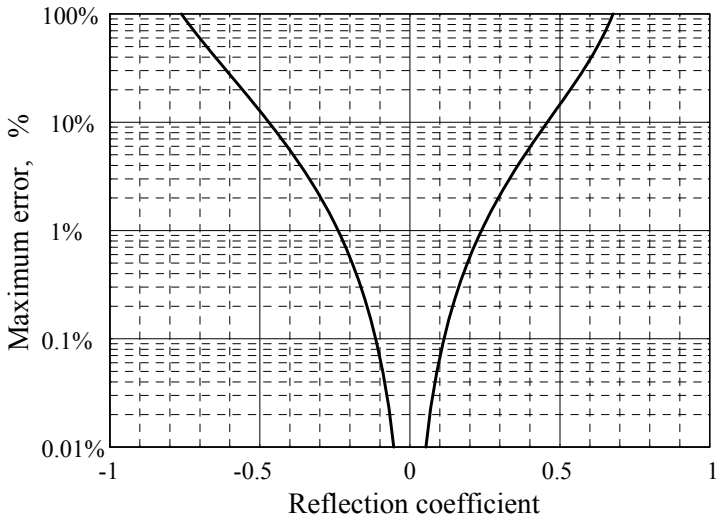

Fig. 25. Maximum error (Eq. 49) vs the reflection coefficient *R* for the linear conductivity profiles in Eq. (48).

6.1 Photothermal depth profiling

Photothermal depth profiling is usually applied to materials subjected to thermal (such as hardening) [47,51], mechanical (such as grinding) [52] or chemical treatments of the surface which exhibit a depth dependence of the thermal conductivity *k(z)* and diffusivity *D(*z), due to the structural modifications in near-surface layers. Photothermal depth profiling allows to reconstruct the thermal conductivity and/or diffusivity depth profiles by monitoring the photothermal signal (photothermal radiometry or photothermal deflection) in the following situations:

(a) depth profiling in frequency domain: the specimen is illuminated by a wide pump laser beam modulated at an adjustable frequency *f*. The photothermal radiometric signal is measured vs the frequency.
(b) depth profiling using lateral scan: the specimen is illuminated by a focused pump laser beam modulated at some frequency *f*. The photothermal deflection signal is measured as a function of the distance from the heating point.
(c) depth profiling in time domain: the specimen is illuminated by a wide pump pulsed laser beam. The photothermal radiometric signal is measured as a function of the time delay from the pulse.

The general idea is to generate at the surface thermal waves (cases *a*,*b*) or a thermal pulse (case *c*) by periodical, or pulsed, laser heating. The thermal waves, or the pulse, penetrate inside the sample, are subjected to a backscattering phenomenon due to the thermal effusivity changes, and come back towards the surface. The surface temperature, resulting from the superposition between the main field and the backscattered field, is eventually detected by photothermal radiometry [7] or by photothermal deflection technique [13-15]. Therefore the photothermal signal contains the information on the thermal depth profiles, which may be reconstructed by simply comparing theory with experiment, for the surface temperature T_{surf} or for any related photothermal signal.

The theoretical value of T_{surf} may be provided by different models of heat diffusion in inhomogeneous materials, when *k(z)* and *D(z)* are known *(direct problem*). Unfortunately many rigorous models allow calculating T_{surf} by using recursive or numerical algorithms, in which a clear relationship between T_{surf} and the thermal parameters is lost. Consequently the depth profile reconstruction (*inverse problem)* consists of a huge set of attempts for fitting T_{surf} by trying all the reasonable profiles. Several procedures have been introduced in the past to optimize such heuristic fitting procedure:

(a) in the frequency domain H.G.Walther et al use a stepwise least squares fit to reconstruct a polygonal best approximation to the conductivity profile [47,51,53], C.Glorieux et al use a neural network approach to find the best fit [54], J.Fivez et al use an inverse procedure to find the Taylor expansion parameters of the conductivity profiles [55], J.F.Power et al use an inverse

Green's function method [56,57], A.Mandelis et al use a Hamilton/Jacobi based model useful for weak scattering [42,58], and Kolarov et al use a thermal wave impedance based model [50].

(b) in the spatial domain H.J.Vidberg applied the inverse scattering method to reconstruct both thermal conductivity and heat capacity depth profiles [59], and H.G.Walther et al use the conjugate gradient method to optimize the fit [60].

(c) in the time domain J.C.Krapez et al reconstruct the effusivity depth profile [61,62], and C. Glorieux et al use the neural network approach to find the best fit [63].

In the following we refer to an inversion procedure based on the *thermal backscattering* model of heat conduction well described by Eqs.(46) and (47) [30, 64-67]. Without loosing generality we restrict our study to the case (a). In this case the specimen is illuminated by a wide pump laser beam, which is modulated at the frequency *f* so to generate a plane thermal wave useful to investigate the internal thermal properties. In particular the frequency *f*, drives the penetration depth $\ell = \sqrt{D/\pi f}$ of the thermal waves (*D* is the thermal diffusivity): for high frequency the induced thermal waves have a short penetration and may investigate the surface thermal properties; on the contrary, for low frequency, the thermal waves have a high penetration, and may investigate deeper layers. Obviously the whole thermal depth profile may be reconstructed by considering the photothermal signal in the whole frequency range. According to the thermal wave backscattering theory (TWBS) a clear direct relationship between the effusivity profile e*(z)* and the photothermal radiometry frequency spectrum *S(f)* may be found as follows.

(a) By inverting Eq.(46), for the inhomogeneous sample under test, one obtains

$$\Gamma(0,f) = \frac{\dfrac{\widetilde{T}_{surf}\, e_{surf}\sqrt{j\omega}}{I} - 1}{\dfrac{\widetilde{T}_{surf}\, e_{surf}\sqrt{j\omega}}{I} + 1} \tag{50}$$

(b) If one repeats the same experiment on a reference homogeneous sample keeping constant the fluency I, the reference surface temperature should be $\widetilde{T}_{ref} = I \big/ e_{ref}\sqrt{j\omega}$, where e_{ref} is the effusivity of the reference sample

(c) If one combines the two previous formula, obtains

$$\Gamma(0,f) = \frac{\dfrac{\widetilde{T}_{surf}\, e_{surf}}{\widetilde{T}_{ref}\, e_{ref}} - 1}{\dfrac{\widetilde{T}_{surf}\, e_{surf}}{\widetilde{T}_{ref}\, e_{ref}} + 1} \tag{51}$$

which is a simple differential expression made not containing the fluency *I*.

(d) by assuming the photothermal radiometry frequency spectrum *S(f)* proportional to the surface temperature, and by using a normalization for the frequency spectrum as follows $S_{norm}(f) = \dfrac{S(f)}{S_{ref}(f)}\dfrac{e_{surf}}{e_{ref}}$, therefore Eqs.(47) and (51) become

$$\frac{S_{norm}(f)-1}{S_{norm}(f)+1} = -\int_0^{\infty} \frac{d\ln(e(z))}{2dz} \exp\left[-2(1+j)\sqrt{\pi f}\int_0^z \frac{d\delta}{\sqrt{D(\delta)}}\right] dz \tag{52}$$

which is the desired relationship between $S_{norm}(f)$ and e(z). The integral in Eq.(52) may be simplified by replacing the real depth z with the reconstruction depth z_{rec}, fulfilling the condition $z_{rec}(z)=\int_0^z d\delta\sqrt{\frac{D_{rec}}{D(\delta)}}$ with D_{rec} a constant. Thus Eq.(52) is transformed into

$$\frac{S_{norm}(f)-1}{S_{norm}(f)+1}=-\int_0^{\infty}\frac{d\ln(e(z_{rec}))}{2dz_{rec}}\exp\left[-2(1+j)z_{rec}\sqrt{\frac{\pi f}{D_{rec}}}\right]dz_{rec} \tag{53}$$

It is worth noting that any inversion procedure from Eq. (53) may only reconstruct the thermal effusivity depth profile $e(z_{rec})$ as a function of z_{rec} which unfortunately differs from z. However in many applications one may assume the heat capacity constant, so to establish a link between effusivity, conductivity and diffusivity depth profiles. In such a case, once $e(z_{rec})$ is calculated from Eq. (53), one may obtain the function $z(z_{rec})$ by solving $dz/dz_{rec}=e(z_{rec})/e_{rec}$, and consequently, combining $e(z_{rec})$ with $z(z_{rec})$ the real effusivity profile $e(z)$ is worked out. The main problem is now the inversion of the integral in Eq. (53). If one measures the thermal reflectivity for N different frequencies, and consider for the thermal effusivity profile the number L of reconstruction depths z_{rec}, the integral in Eq. (53) may be replaced by the summation and finally reduced to a linear system. The problem of reconstruction consists now in solving such ill-posed system of $2N$ equations (one set for the real and another set for the imaginary part of Γ) in L unknown quantities by the help of the Singular Value Decomposition mathematical tool (SVD). *SVD* analyses the matrix *Lx2N* in terms of eigenvectors and relative eigenvalues, and uses just a few of them for the inversion. In fact the use of the lower eigenvalues generally leads to a clear instability in the reconstruction. The criterion of selection consists in the definition of a threshold eigenvalue λ_{th}, and is given by using for the inversion only eigenvalues larger than this threshold. On one hand this procedure allows to reconstruct stable profiles, but on the other hand it limits the spatial resolution in reconstruction which strongly depends on the choice of λ_{th}.

As a theoretical example we report the results of some numerical simulation on a sample made of two layers: film + bulk. The diffusivity of the film is D=0.09cm^2/s, while for the bulk D=0.2cm^2/s. We have chosen a "*step*" profile just to test the performance of TWBS. This is the worse profile to be reconstructed for any inversion procedure, and is useful to check the limit of validity of Eq.(52). In Fig. 26 the ratio $\frac{S_{norm}(f)-1}{S_{norm}(f)+1}$ is shown as a function of frequency.

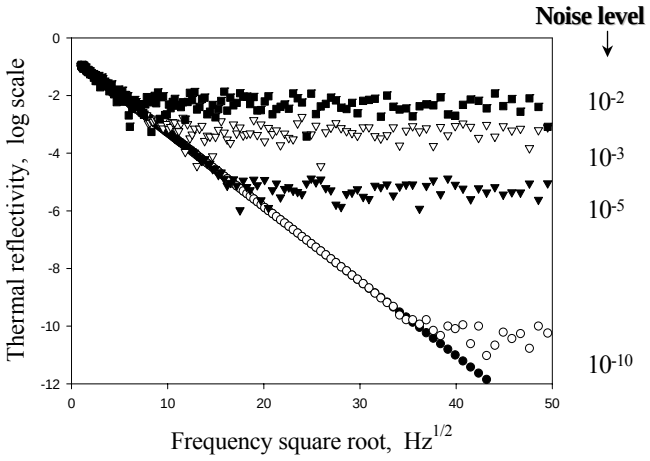

Fig. 26. thermal reflectivity (log scale) vs frequency square root for many noise levels (10^{-2}, 10^{-3}, 10^{-5}, 10^{-10}).

The curves refer to different levels of Gaussian noise. The ideal curve for noiseless data must be a straight line in the log plot. The presence of noise reduces the information content of the curve, damaging definitively the high frequency regime. The corresponding thermal diffusivity reconstructions are shown in Fig. 27. As the noise level increases, some oscillations appear in the reconstruction. In fact the loss of information seen in Fig. 26 must reflect the loss of spatial resolution in Fig. 27.

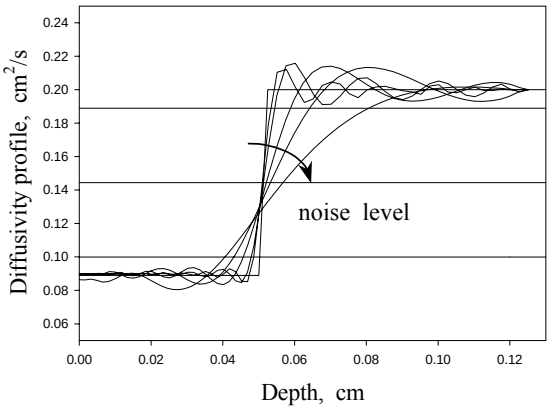

Fig. 27. Thermal diffusivity reconstructions by SVD for the same different levels of noise of Fig. 1 (10^{-2}, 10^{-3}, 10^{-5}, 10^{-10}).

As a experimental example of the depth profiling in frequency regime, we may show some experimental results on hardened steel materials. The hardening process is a thermal cycle made of a heating process to reach the complete *austenization* of the steel, and a very fast cooling to obtain the *martensitic* structure, which exhibits a higher hardening property. In many industrial applications the hardening process allows to increase the hardening of the steel, transforming into *martensite* the surface layers up to a suitable depth L in the millimeter range (*hardening depth*), depending on the applications. Since *martensite* has lower thermal conductivity than *austenite*, the hardened steels are macroscopically thermally inhomogeneous and may be described by a thermal conductivity depth profile *k(z)* corresponding to the in-depth hardening process.

Concerning the other thermal parameters, the heat capacity has no significant changes from *austenite* to *martensite*, and therefore may be assumed constant: this means that both conductivity and diffusivity profiles are proportional one to each other.

We show photothermal radiometric signals measured for three samples:

(a) One hardened steel sample thermally inhomogeneous;
(b) The same sample of *case a*, after the cut of a 140μm-thick surface layer. In practice it may be considered as a new inhomogeneous sample.
(c) One homogeneous steel sample used as a reference.

The photothermal radiometric signals of *cases a,b* should be normalized to the *case c*; the normalization is a standard step for the inversion as described below, and moreover allows to reduce the systematic errors in the measurement. The normalized signals $S_{norm}(f)$ of *case a* (+) and *case b* (□) are plotted vs the frequency square root: the amplitude ratio is in Fig. 28a, while the phase contrast is in Fig. 28b. It is worth noting that for both *cases a* and *b,* the phase contrast is positive, corresponding to the condition $k_{surf} < k_{bulk}$, as expected in any hardening process. By using the SVD procedure, the normalized signals in Figs. 28 may be inverted in order to reconstruct the best diffusivity depth profiles for both *cases a* and *b* as plotted in Fig. 29. Since for both *cases a* and *b* the sample is the same, if one shifts appropriately the reconstructed depth profiles of 140 μm (as it is done in Fig. 29), the two profiles should superpose. The slight differences visible on the figure give a quantitative information of the error of the procedure. As a further validation note in Figs. 28 the good

quality of the fit between the experimental data (symbols) and the continuous curves corresponding to the profiles in Fig. 29. As a conclusive remark one may observe that the hardening process corresponds to a change of diffusivity from $D_{bulk}=0.2cm^2/s$ to $D_{surf}=0.08cm^2/s$.

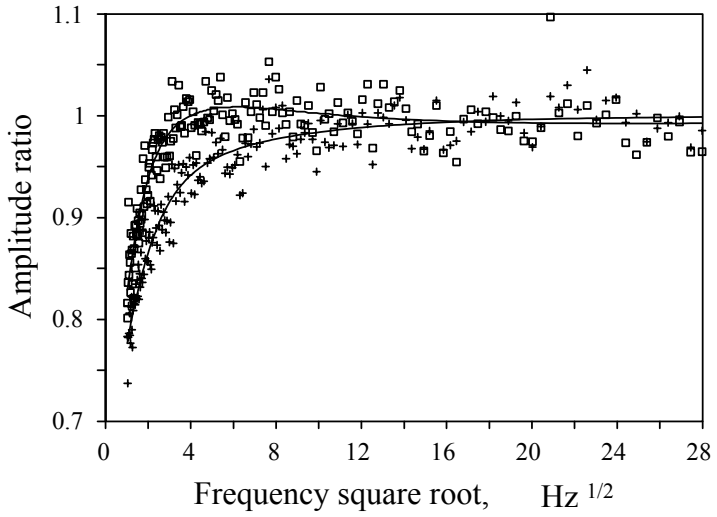

Fig. 28a. Amplitude of the radiometric signal vs frequency square root. The symbols represent the experimental data: (+) hardened steel sample; (□) the same hardened steel sample, after the cut of a 140μm-thick surface layer; (full lines) best fit by SVD corresponding to the depth

profiles in Fig. 29.

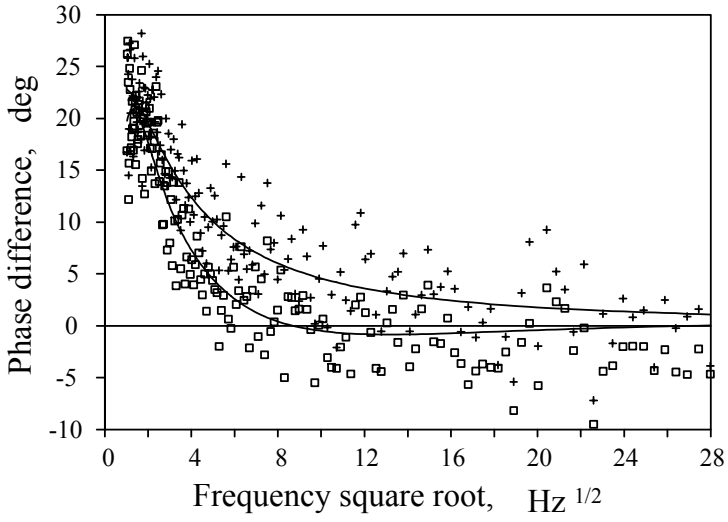

Fig. 28b. Phase difference (deg.) vs frequency square root: the symbols represent the experimental data: (+) hardened steel sample; (□) the same hardened steel sample, after the cut of a 140μm-thick surface layer; (full lines) best fit by SVD corresponding to the depth profiles in Fig. 29.

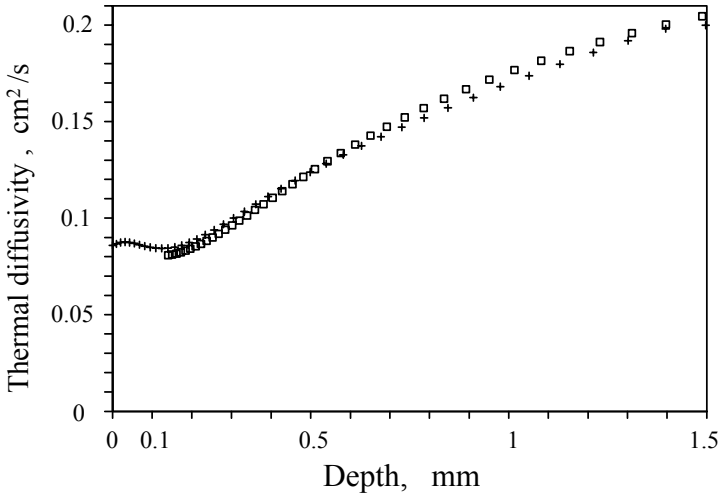

Fig. 29. Diffusivity depth profiles from the radiometric data in Fig. 28. The reconstruction is performed by using the TWBS theory, and the SVD algorithm: (+) hardened steel sample; (□) the same hardened steel sample, after the cut of a 140μm-thick surface layer.

7. Conclusions

In this paper we have reviewed the basis of the thermal wave physics, focusing the attention not only on many theoretical aspects but also on the main applications for the nondestructive material testing.

References

[1] Lord Kelvin. "The reduction of observations of underground temperature." Trans. Roy. Soc. Edin, Vol. 22, 405 (1861).
[2] A. J. Ångström, "New method of determining the thermal conductivity of bodies." Phil Mag. Vol. 25, 130 (1863).
[3] C. A. Jr. Bennett, R. R. Patty, "Thermal wave interferometry: a potential application of the photoacoustic effect." Appl. Opt. Vol. 21, 49 (1982).
[4] A. Rosencwaig, A. Gersho. "Thermal-wave imaging." Science Vol. 218, 223-228 (1982).
[5] H. S. Carslaw, J. C. Jaeger. Conduction of heat in solids, Oxford University Press London (1959).
[6] A. Mandelis, "Green's function in thermal wave physics: cartesian coordinate representations." J. Appl. Phys. Vol.78, No.2, 647-655 (1995).
[7] D. P. Almond, P.M. Patel, Photothermal Science and Techniques, Chapman & Hall (1996).
[8] R. Li Voti, "La tecnica di deflessione fototermica: principio ed applicazioni" Ph.D. Thesis (1996).
[9] M. Bertolotti, G. L. Liakhou, R. Li Voti, S. Paoloni, C. Sibilia. "Thermal wave reflection and refraction: theoretical and experimental evidence" J. Appl. Phys Vol. 85, No. 7, 3540-3545 (April 1999).
[10] M. Bertolotti, R. Li Voti, C. Sibilia, G. L. Liakhou. "Analysis of defects in multilayers through photothermal deflection technique." Specification, Production, and Testing of Optical Components and Systems [Glasgow, Scotland, UK, May 1996] SPIE Vol. 2775, 370-379 (1996).
[11] P. M. Patel, D. P. Almond, H. Reiter. "Thermal wave detection and characterisation of sub-surface defects." Appl. Phys B. Vol. 43, 9-15 (1987).
[12] R. L. Thomas, J. J. Pouch, W. H. Wong, L. D. Favro, P. K. Kuo, A. Rosencwaig. "Subsurface flaw detection in metals by photoacoustic microscopy." J.Appl. Phys. Vol. 51, No. 2, 1152-1156 (1980).

[13] W. B. Jackson, N. M. Amer, A. C. Boccara, D. Fournier. "Photothermal deflection spectroscopy and detection." Applied Optics. Vol. 20, No. 8, 1333-1344 (1981).
[14] A. C. Boccara, D. Fournier, W. Jackson, N. M. Amer, "Sensitive photothermal deflection technique for measuring absorption in optically thin media" Optics Letters. Vol. 5, No. 9, 377-379 (1980).
[15] M. Bertolotti, G. L. Liakhou, R. Li Voti, S. Paoloni, C. Sibilia. "Analysis of the photothermal deflection technique in the surface reflection scheme: Theory and experiment." J. Appl. Phys Vol. 83, No. 2, 966-982 (1998).
[16] M. Bertolotti, G. L. Liakhou, R. Li Voti, S. Paoloni, C. Sibilia, N. Sparvieri. "A Cryostatic set-up for the low temperature measurements of thermal diffusivity with the photothermal method." Rev. Sci. Instrum. Vol. 66, No. 12, 5598-5602 (1995).
[17] M. Bertolotti, G. L. Liakhou, R. Li Voti, Ruo Peng Wang, C. Sibilia, A. V. Syrbu, V. P. Yakovlev: "An experimental and theoretical analysis of the temperature profile in semiconductor laser diodes using the photodeflection method." Meas. Sci. Technol. Vol. 6, 1278-1290 (1995).
[18] Y. S. Touloukian, R. W. Powell, C. Y. Ho, M. C. Nicolaou. Thermophysical properties of matter, Vol. 10 Plenum New York, (1973).
[19] C. B. Reyes, J. Jaarinen, L. D. Favro, P. K. Kuo, R. L. Thomas. in Review of Progress in Quantitative Nondestructive Evaluation, edited by D. O. Thompson and D. E. Chimenti Vol. 6 Plenum, New York, 271 (1987).
[20] M. Bertolotti, R. Li Voti, G. Liakhou, C. Sibilia, "On the photodeflection method applied to low thermal diffusivity measurements" Rev. Sci. Instrum. Vol. 64, No. 6, 1576 (1993).
[21] M. Bertolotti, V. Dorogan, G. Liakhou, R. Li Voti, S. Paoloni, C. Sibilia "New photothermal deflection method for thermal diffusivity measurement of semiconductor wafers" Rev. Sci. Instrum. Vol. 68, No. 3, 1521-1526 (1997).
[22] H. Coufal, P. Hefferle. "Thermal diffusivity measurements of thin films with a pyroelectric calorimeter." Appl. Phys A Vol. 38, 213-219 (1985).
[23] A. Mandelis, "Theory of photothermal-wave diffraction and interference in condensed media" J. Opt. Soc. Am. A Vol. 6, No. 2, 298-308 (1989).
[24] A. C. Bento, D. P. Almond, "The accuracy of thermal wave interferometry for the evaluation of thermophysical properties of plasma-sprayed coatings." Meas. Sci. Technol printed in UK Vol. 6 1022-1027 (1995).
[25] M. Bertolotti, G. L. Liakhou, R. Li Voti, S. Paoloni, C. Sibilia. "Thickness measurement by photothermal deflection method: basic influence of surface conductance." Progress in Natural Science [Nanjing, China, June 1996] Suppl. to Vol. 6, S-309-312 (1996).
[26] J. Opsal, A. Rosencwaig. "Thermal wave detection and thin film thickness measurements with laser beam deflection." Appl. Opt. Vol. 22, No. 20, 3169-3176 (1983).
[27] L. Fabbri, F. Cernuschi. "Finite laser beam size effects in thermal wave interferometry" J. Appl. Phys Vol. 82, 5305-5307 (1997).
[28] H. G. Walther, T. Kitzing, "Systematic errors of locally resolved photothermal radiometric measurements." J. Appl. Phys. Vol. 84, 1163-1167 (1998).
[29] M. Bertolotti, M. Firpo, R. Li Voti, S. Paoloni, C. Sibilia, F. Tani, G. L. Liakhou. "Thermal characterization of a multilayer material." Progress in Natural Science [Nanjing, China, June 1996] Suppl. to Vol. 6, S-219-222 (1996).
[30] R. Li Voti, M. Bertolotti, C. Sibilia. "Thermal conductivity and diffusivity depth profiles by photothermal technique: the direct and inverse problems" III International Whorkshop – Advances in signal processing for NDE of materials [Quebec City, Canada August 1997] Ed. B. Djordjevic, H. Dos Reis, Vol. 3, 379-386 (1998).
[31] J. Shen, A. Mandelis, "Thermal-wave resonator cavity" Rev. Sci. Instrum. Vol. 66, 4999 (1995).
[32] M. Bertolotti, G. L. Liakhou, R. Li Voti, S. Paoloni, C. Sibilia, "Thermal wave resonator: in situ investigation by photothermal deflection technique." Int. Journal of Thermophysics [Boulder, Colorado, June 1997] printed by Catherine Press Belgium Vol. 19, No. 2, 603-613 (1998).
[33] J. Shen, A. Mandelis, T. Ashe. "Pyroelectric thermal-wave resonant cavity: a precision thermal diffusivity sensor for gases and vapors." Int. Journal of Thermophysics [Boulder, Colorado, June 1997] printed by Catherine Press Belgium Vol.19, No. 2 (1998).
[34] J. Opsal, A. Rosencwaig. "Thermal-wave depth profiling." J. Appl. Phys. Vol. 53, No. 6 4240-

4246 (June 1982).
[35] L. C. Aamodt, J. C. Murphy. "Thermal effects in materials with continuously varying optical and thermal properties in one dimension." Can. J. Phys Vol. 64, 1221-1229 (1986).
[36] P. Grossel, F. Depasse. "Alternating heat diffusion in thermophysical depth profiles: multilayers and continuos descriptions." J.Phys.D: Appl. Phys Vol. 31 printed in UK 216-223 (1998).
[37] D. Josell, A. Cezairliyan, D. Van Heerden, B. T. Murray. "An integral solution for thermal diffusion in periodic multilayer materials: application to Iron/Copper multilayers." Int. Journal of Thermophysics printed in Belgium Vol. 18, No. 3, 865-885 (1997).
[38] A. Salazar, A. Sanchez-Lavega, J. M. Terron. "Effective thermal diffusivity of layered materials measured by modulated photothermal techniques" J. Appl. Phys. Vol. 84, 3031-3041 (September 1998).
[39] A. Mandelis, Photoacoustic and thermal wave phenomena in semiconductors North-Holland, N.Y. (1987).
[40] J. A. Sell, Photothermal investigation of solids and fluids Academic Press, Boston (1989).
[41] C. Glorieux, J. Fivez, J. Thoen. "Photoacoustic investigation of the thermal properties of layered materials: calculation of the forward signal and numerical inversion procedure." J. Appl. Phys. Vol. 73, No. 2, 684-690 (January 1993).
[42] A. Mandelis, F. Funak, M. Munidasa. "Generalized methodology for thermal diffusivity depth profile reconstruction in semi-infinite and finitely thick inhomogeneous solids." J. Appl. Phys. Vol. 80, 5570-5578 (November 1996).
[43] U. Seidel, T. T. N. Lan, H. G. Walther, B. Schmitz, J. Geerkens, G. Goch. "Quantitative characterization of material inhomogeneities by thermal waves." Opt. Eng. Vol. 36, 376-390 (February 1997).
[44] M. Bertolotti, R. Li Voti, G. L. Liakhou, S. Paoloni, C. Sibilia. "A new approach to the photothermal depth profiling in frquency domain: theory and experiment" Photoacoustic and Photothermal Phenomena [Rome, Italy, August 1998] AIP Conference Proceedings 463, 24-26 (1999).
[45] M. Bertolotti, G. L. Liakhou, R. Li Voti, S. Paoloni, C. Sibilia, V. Violante. "Thermal conductivity depth profiling in inhomogeneous compounds by photothermal techniques" Microscale heat transfer [Futuroscope, July 1998] Eurotherm Seminar n°57 (1999).
[46] J. Fivez, J. Thoen. "Thermal waves in materials with linearly inhomogeneous thermal conductivity." J. Appl. Phys. Vol. 75, 7696 (December 1994).
[47] T. T. Lan U. Seidel, H. G. Walther. "Theory of microstructural depth profiling by photothermal measurements." J. Appl. Phys Vol. 77, 4739-4745 (1995).
[48] J. Fivez, J. Thoen. "Thermal waves in materials with inhomogeneous thermal conductivity: an analytical approach." J. Appl. Phys. Vol. 79, 2225-2228 (March 1996).
[49] J. Fivez, J. Thoen. J. Appl. Phys. Vol. 81, 2963 (1997).
[50] R. Kolarov, T. Velinov. "Real-time depth profile reconstruction of the thermal conductivity of inhomogeneous solids." J. Appl. Phys Vol. 83, No. 4, 1878-1883 (February 1998).
[51] U. Seidel, T. T. N. Lan, H. G. Walther, B. Schmitz, J. Geerkens, G. Goch. "Quantitative characterization of material inhomogeneities by thermal waves." Opt. Eng. Vol. 36, 376-390 (February 1997).
[52] S. Malkin, J. E. Ritter, "Grinding mechanism and strength degradation for ceramics." J. Eng. Indust. Vol. 111, 167-174 (1989).
[53] T. T. N. Lan, U. Seidel, H. G. Walther, G. Goch, B. Schmitz. "Experimental results of photothermal microstructural depth profiling." J. Appl. Phys Vol. 78, No. 6, 4108-4111 (1995).
[54] C. Glorieux, J. Thoen. "Thermal depth profile reconstruction by neural network recognition of the photothermal frequency spectrum" J. Appl. Phys. Vol. 80, No. 11, 6510-6515 (1996).
[55] J. Fivez, J. Thoen. "Thermal waves in materials with inhomogeneous thermal conductivity: an analytical approach" J. Appl. Phys. Vol. 79, No. 5, 2225-2228 (March 1996).
[56] J. F. Power, Opt. Engin Vol. 36, 487-503 (1997).
[57] J. F. Power "A survey of current issues in inverse problem theory as applied to thermal wave imaging." Photoacoustic and Photothermal Phenomena [Rome, Italy, August 1998] AIP Conference Proceedings 463, 3-7 (1999).
[58] M. Munidasa, F. Funak, A. Mandelis. "Application of a generalized methodology for

quantitative thermal diffusivity depth profile reconstruction in manifactured inhomogeneous steel-based materials." J. Appl. Phys. Vol. 83, No. 7, 3495-3498 (April 1998).
[59] H. J. Vidberg, J. Jaarinen, D. O. Riska. "Inverse determination of the thermal conductivity profile in steel from thermal surface data." Can. J. Phys. Vol. 64, No. 86, 1178-1183 (1986).
[60] H. G. Walther, T. T. N. Lan, V. Aleshin. "Reconstruction of thermal conductivity depth profiles from photothermal measurements" III International Whorkshop – Advances in signal processing for NDE of materials [Quebec City, Canada August 1997] Ed. B. Djordjevic and H. Dos Reis, Vol. 3, 41-47 (1998).
[61] D. L. Balageas J. C. Krapez, P. Cielo. "Pulsed photothermal modeling of layered materials." J. Appl. Phys. Vol. 59, No. 2, 348-355 (January 1986).
[62] J. C. Krapez, "Inversion method for effusivity depth profile retrieval. Application to the characterization of case hardened steel." Unpublished.
[63] C. Glorieux, R. Li Voti, J. Thoen, M. Bertolotti, C. Sibilia. "Depth profiling of thermally inhomogeneous materials by neural network recognition of photothermal time domain data." J. Appl. Phys. Vol. 85, No. 10, 7059-7063 (May 1999).
[64] M. Bertolotti, R. Li Voti, G. L. Liakhou, S. Paoloni, C. Sibilia. "A new approach to the photothermal depth profiling in frquency domain: theory and experiment" Photoacoustic and Photothermal Phenomena [Rome, Italy, August 1998] AIP Conference Proceedings 463, 24-26 (1999).
[65] M. Bertolotti, G. L. Liakhou, R. Li Voti, S. Paoloni, C. Sibilia, V. Violante. "Thermal conductivity depth profiling in inhomogeneous compounds by photothermal techniques" Microscale heat transfer [Futuroscope, July 1998] Eurotherm Seminar n°57 (1999).
[66] M. Bertolotti, R. Li Voti, G. L. Liakhou, S. Paoloni, C. Sibilia, V. Aleshin, H. G. Walther. "Depth profiling using laterally resolved photothermal measurements applied for the estimation of the steel hardness profiles" Photoacoustic and Photothermal Phenomena [Rome, Italy, August 1998] AIP Conference Proceedings 463, 11-13 (1999).
[67] R. Li Voti, G. L.Liakhou, S. Paoloni, E. Scotto, C. Sibilia, M. Bertolotti. "Theory of photothermal depth profiling in time domain" Photoacoustic and Photothermal Phenomena [Rome, Italy, August 1998] AIP Conference Proceedings 463, 37-39 (1999).
[68] C. Glorieux, R. Li Voti, J. Thoen, M. Bertolotti, C. Sibilia. "Analysis of reconstruction errors." Inverse Problems, Vol. 8 (1999).
[69] R. Li Voti, C. Glorieux. "Plausibility study of photothermal depth profiling in frequency domain" Photoacoustic and Photothermal Phenomena [Rome, Italy, August 1998] AIP Conference Proceedings 463, 34-36 (1999).